PFC/RR-83-16

A STUDY OF STRUCTURAL RESPONSES TO PLASMA DISRUPTIONS IN TOROIDAL SHELLS

by

M. S. Tillack

June 1983

Plasma Fusion Center
and the
Department of Nuclear Engineering
Massachusetts Institute of Technology
Cambridge, Massachusetts 02139

Prepared for

EG&G Idaho, Inc.

and

The U.S. Department of Energy
Idaho Operations Office

under

DOE Contract # DE-AP07-79ID0019

A Study of Structural Responses to Plasma Disruptions in Toroidal Shells

Abstract

An efficient set of 1-D computer routines has been developed to analyze the induced currents, pressure loading, and structural response in thin toroidal shells due to externally imposed current and magnetic field transients. The method is used to study the behavior of the Tokamak first wall during plasma disruption. A base case is analyzed and then variations are made to the key parameters to demonstrate important trends. For the base case, peak poloidal strains of 5×10^{-4} *at the inboard edge and bending stresses of .7 MPa at the top and bottom edges are observed.*

The results show significant differences in both the magnitude and spatial variation of loading and structural response for the different cases studied, indicating that certain designs are more resistant to disruptions than others. High aspect ratio designs tend to have low induced strains whereas compact, low aspect ratio designs tend to have large strains and large poloidal asymmetry. Plasma shift is seen to have an influence on both the level of strain and its spatial dependence. The peak bending stress observed with a 25% plasma shift was 10 MPa with peak strain of 6×10^{-4} *in the toroidal, instead of the poloidal direction.*

Contents

Table of Contents 2

List of Figures 4

Publications 5

Nomenclature 7

Chapter 1 Introduction 9

1. Overview of Pressures 10
2. Overview of Stresses 13

Chapter 2 Description of Computational Method 17

1. The Eddy Current Problem 17
2. The Structural Problem 19

Chapter 3 Base Case 24

1. Description of Base Case 24
2. Base Case Results 25

Chapter 4 Variation of Parameters 31

1. Equations Used for Self-Consistency 31
2. Results From Variation of Parameters 32
3. Effect of Large Plasma Shift 33
4. Effects of an Electromagnetic Shield 34

Chapter 5 Conclusions 34

References 41

Appendix A Magnetic Fields 42

Appendix B Structural Equations 43

Appendix C B-Splines as Basis Functions 45

Appendix D Structural Plots for Design Comparison 48

List of Figures

1. Definition of Coordinates

2. Contours of Constant B from a Current Loop

3. B-lines and Equipotentials from a Current Loop

4. Pressurized Torus Displacements

5. Pressurized Torus Moments

6. B-Spline Basis Function and Derivatives

Base Case Profiles:

7. Current vs. Time

8. Radial Pressure vs. Time

9. Current vs. Poloidal Angle

10. Radial Pressure vs. Poloidal Angle

11. Circumferential Pressure vs. Poloindal Angle

12. Base Case Displacements

Effects of Plasma Shift and EM Shield:

13. Radial Pressure Profiles for Plasma Shift

14. Radial Pressure Profiles for EM Shield

15. Structural Response at 20 msec for Plasma Shift

16. Structural Response at 100 msec for Plasma Shift

17. Structural Response at 20 msec for EM Shield

18. Structural Response at 100 msec for EM Shield

PUBLICATIONS UNDER CONTRACT #K-1702 ON FUSION SAFETY

A. General Safety and Risk Assessment

1. M. S. Kazimi et al., "Aspects of Environmental Safety Analysis of Fusion Reactors," MITNE-212, Dept. of Nuclear Engineering, M.I.T. October 1977.

2. R. W. Sawdye, J. A. Sefcik, M. S. Kazimi, "Reliability Requirements for Admissible Radiological Hazards from Fusion Reactors," Trans. Am. Nucl. Soc. 27, 65-66, November 1977.

3. R. W. Sawdye and M. S. Kazimi, "Application of Probabilistic Consequence Analysis to the Assessment of Potential Radiological Hazards of Fusion Reactors," MITNE-220, Dept. of Nuclear Engineering, M.I.T., July 1978.

4. R. W. Sawdye and M. S. Kazimi, "Fusion Reactor Reliability Requirements Determined by Consideration of Radiological Hazards," Trans. Am. Nucl. Soc. 32, 66, June 1979.

5. M. S. Kazimi and R. W. Sawdye, "Radiological Aspects of Fusion Reactor Safety: Risk Constraints in Severe Accidents," J. of Fusion Energy, Vol. 1, No. 1, pp. 87-101, January 1981.

6. S. J. Piet, M. S. Kazimi and L. M. Lidsky, "Potential Consequences of Tokamak Fusion Reactor Accidents: The Materials Impact," PFC/RR-82-19, Plasma Fusion Center, M.I.T., June 1982.

7. S. J. Piet, V. J. Gilberti, "FUSECRAC: Modifications of CRAC for Fusion Application," Nuclear Eng. Dept. and Plasma Fusion Center, M.I.T., PFC/RR-82-20, June 1982.

8. M. S. Kazimi, "Safety and Risk Targets for Fusion Energy," Societe Francaise de Radioprotection 10th Annual Congres, Avignon, France, Oct. 18-22, 1982.

9. M. S. Kazimi, "Safety Methodology and Risk Targets," in Proc. of 1982 IAEA Workshop on Fusion Safety, IAEA-TECDOC-277, 1983.

B. Lithium Reactions

1. D. A. Dube, M. S. Kazimi and L. M. Lidsky, "Thermal Response of Fusion Reactor Containment to Lithium Fire," 3rd Top. Meeting on Fusion Reactor Technology, May 1978.

2. D. A. Dube and M. S. Kazimi, "Analysis of Design Strategies for Mitigating the Consequences of Lithium Fire witin Containment of Controlled Thermonuclear Reactors, MITNE-219, Dept. of Nuclear Engineering, M.I.T., July 1978.

3. M. S. Tillack and M. S. Kazimi, "Development and Verification of the LITFIRE Code for Predicting the Effects of Lithium Spills in Fusion Reactor Containments," PFC/RR-80-11, Plasma Fusion Center, M.I.T., July 1980.

4. P. J. Kraine and M. S. Kazimi, "An Evaluation of Accidental Water-Reactions with Lithium Compounds in Fusion Reactor Blankets," PFC/RR-81-26,, Plasma Fusion Center, M.I.T., July 1981.

5. M. S. Tillack and M. S. Kazimi, "Modelling of Lithium Fires," Nuclear Technology/Fusion, Vol. 2, No. 2, pp. 233-245, April 1982.

6. V. J. Gilberti and M. S. Kazimi, "Modeling of Lithium and Lithium-Lead Reactions in Air Using LITFIRE," PFC/RR-82-08, Plasma Fusion Center, M.I.T., January 1983.

7. E. Yachimiak, V. Gilberti, and M. S. Tillack, "LITFIRE User's Guide," Nuclear Eng. Dept. and Plasma Fusion Center, M.I.T., PFC/RR-82-11, June 1983.

C. Tritium

1. S. J. Piet and M. S. Kazimi, "Uncertainties in Modeling of Consequences of Tritium Release from Fusion Reactors," PFC/TR-79-5, Plasma Fusion Center and Nucl. Eng. Dept., M.I.T., July 1979.

2. M. J. Young and S. J. Piet, "Revisions to AIRDOS-II," PFC/TR-79-8, Plasma Fusion Center and Nucl. Eng. Dept., M.I.T., August 1979.

3. S. J. Piet and M. S. Kazimi, "Implications of Uncertainties in Modeling of Tritium Releases from Fusion Reactors," Proc. Tritium Technology in Fission, Fusion and Isotopic Applications, April 1980.

4. D. R. Hanchar and M. S. Kazimi, "Tritium Permeation Modelling of a Conceptual Fusion Reactor Design," PFC/RR-81-27, Plasma Fusion Center, M.I.T., July 1981.

D. Electromagnetic Consideration

1. R. W. Green and M. S. Kazimi, "Safety Considerations in the Design of Tokamak Toroidal Magnet Systems," Trans. ANS 32, 69, June 1979.

2. R. W. Green and M. S. Kazimi, "Aspects of Tokamak Toroidal Magnet Protection," PFC/TR-79-6, Plasma Fusion Center, M.I.T., July 1979.

3. M. S. Tillack, "A Study of Structural Responses to Plasma Disruptions in Toroidal Shells," Dept. of Nucl. Eng. and Plasma Fusion Center, M.I.T., PFC/RR-83-16, June 1983.

E. Others

1. M. S. Kazimi, "IAEA Workshop on Fusion Safety March 23-27, 1981, Vienna, Austria," J. of Fusion Energy, Vol. 1, No. 3, pp. 241-243, 1981.

Nomenclature

a	minor radius
A	magnetic vector potential
B_p	poloidal magnetic field (Tesla)
B_t	toroidal magnetic field (Tesla)
B_v	equilibrium vertical magnetic field
c	speed of sound in a material
D	flexural rigidity
E	modulus of elasticity or electric field
E(k)	complete elliptic integral of the second kind
h	shell thickhess
I	current (amps)
j or J	current density (amps/m^2)
K	surface current density (amps/m) or bending rigidity
K(k)	complete elliptic integral of the first kind
L	self inductance
M	general mutual inductance
M_o	mutual inductance with the source current
M_θ	toroidal moment (Nm/m)
M_ϕ	poloidal moment (Nm/m)
$M_{\phi\theta}$	twist (Nm/m)
N_θ	toroidal stress resultant (N/m)
N_ϕ	poloidal stress resultant (N/m)
p_a	radial pressure in toroidal coordinate system
p_r	radial pressure in cylindrical coordinates
p_ϕ	poloidal pressure
q_a	quality factor at a
Q_ϕ	poloidal shear (N/m)
r	distance from axis of symettry
R	major radius or resistance
u or w	radial displacement
v	poloidal displacement
V	voltage
W	reactor total power output

Nomenclature, continued

$\langle\beta_t\rangle$	average toroidal beta
$\langle\beta_t\rangle$	average poloidal beta
ϵ_θ	toroidal strain
ϵ_ϕ	poloidal strain
$\epsilon_{\phi\theta}$	shear strain
η	resistivty (ohm-m)
θ	toroidal angle coordinate
ι	rotational transform
μ_o	permeability of free space
ν	Poisson's ratio
ρ	material density
σ_b	bending stress
ϕ_e	poloidal angle coordinate used in eddy current analysis
ϕ_s	poloidal angle coordinate used in structural analysis
χ_θ	theta curvature
χ_ϕ	phi curvature
ω	frequency
Ω	dimensionless frequency
$(\ )'$	$d(\ )/d\phi$

1. Introduction

Recent fusion reactor studies have concentrated on increasingly detailed designs of the first wall/blanket/shield region. One area which has received particular attention is an engineering analysis of the effects of major plasma disruptions in tokamaks. Currently there is a general agreement that disruptions are one of the limiting influences on first wall lifetime.

Disruptions generate two very different effects in the first wall. The most widely studied is the effect of particle and radiation fluxes, including thermal strains, sputtering, and phase change. One good example of design against these problems is FED. In order to protect the inboard surface of the first wall, the FED design incorporates a large number of graphite armor tiles designed to absorb the plasma kinetic energy.[1]

Other potentially serious effects arise from the rapid termination of plasma current during disruptions. Large electromagnetic forces may be generated by induced eddy currents in the first wall and blanket region. If the circulating current paths are eliminated, then large voltages may be generated, resulting in the possibility of arcing. Relatively less work has been devoted to these concerns as opposed to thermal and particle effects, however there are some notable examples in the literature. In the STARFIRE design, net forces were calculated on the limiter using the EDDYNET code.[2] The FED/INTOR design accounts for the pressure loading on the first wall as well as in the poloidal limiter and considers the possibility of arcing between sectors.[3,4] In either of these cases, the resulting structural response due to the loading was not considered.

The present work attempts to systematically document the general behavior of the first wall, in terms of induced currents and forces, using a simple approach with 1-D currents and 2-D fields. The plasma current is approximated by a single filament located inside the torus, with an exponential decay after $t = 0$. This modeling is crude, but the exact details of the current profile evolution are not well known. The calculation includes a quantitative treatment of structural response, including displacements, moments, shears, and strains. This part of the

problem is fully 1-D, with toroidal axisymmetry and the poloidal angle being the independent variable. Most of the spatial details of the problem are ignored in order to simplify the analysis. Consequently, gross design variations can be quickly analyzed and contrasted. This includes variations in aspect ratio, plasma current, vertical field, and several other averaged design parameters. Other effects which were studied include an outward plasma shift and a second conducting shell outside the first wall to model the multiplier, breeder, and other structure behind the first wall.

1.1. Overview of Pressures

The first step in the analysis is the determination of induced currents and pressures arising from J $\times$ B forces. The eddy current problem has 1-D currents directed along θ and 2-D magnetic fields which contain both R- and z-components.

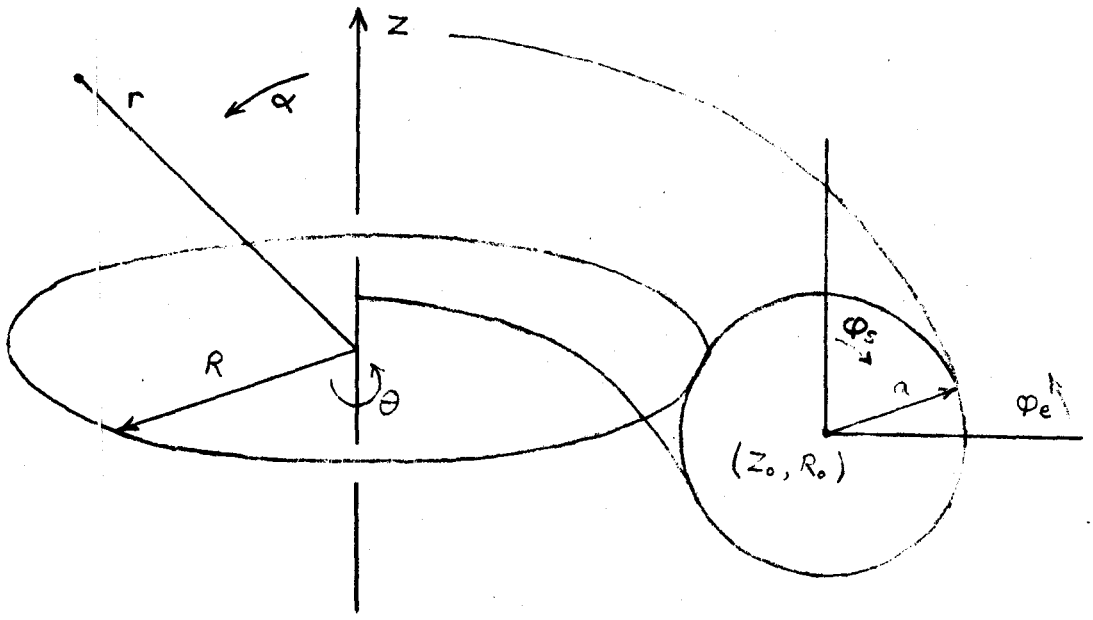

Fig. 1 Definition of Coordinates

(see fig 1.) The structure being analyzed includes a conducting toroidal shell whose volume contains current-carrying plasma. This current is called the source or driving current. When the plasma currents experience a transient, there are currents induced in the shell which attempt to maintain the field pattern unchanged. These currents are called the induced or structural currents. If the magnetic diffusion time of the torus is long compared to the transient time constant, then the structural currents are large and shield the region outside the torus from the transient. In this case the structural currents die away slowly due to the low resistance of the structure. This is the case for the examples studied in this document.

For a source current at the center of the torus, the induced currents are peaked on the part of the shell closest to the major axis. The main reason for this is the lower resistance of the inner edge due to a shorter path length around the torus. In addition, the field due to a current loop is larger inside the loop, therefore the linked fluxes are larger on the inside of the shell (see figs 2 and 3 and Appendix A). The result is larger induced currents. Of course, if the source current is shifted outward with respect to the shell axis, then this would not necessarily hold true. A shifted current example is analyzed later for comparison. Even disregarding this non-uniform field effect, at early times in the transient the flux through the central hole is well shielded by the inner edge, resulting in another reason for the existence of peaked induced currents.

The forces generated by a disruption can be generalized into three main components:

1. Minor Radius Compression

The induced currents always flow in the same direction as the source current. This results in a minor radius compressive force due to both shell current interaction with the shell current field ("self-interactions") and shell current interaction with the source current field ("source-interactions").

2. Hoop Force Expansion

The hoop force attempts to expand the shell towards a larger major radius. On the inboard side it is aligned with the major radius component of the

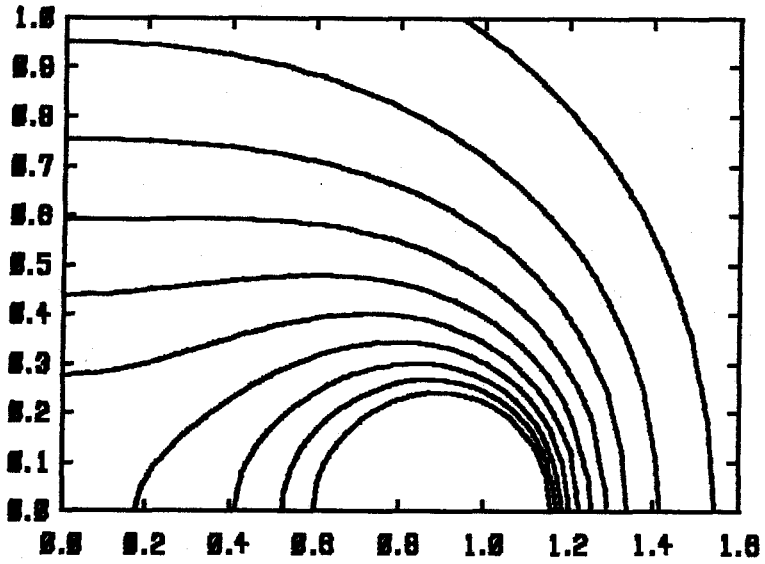

FIGURE 2. Contours of Constant B from a Current Loop.

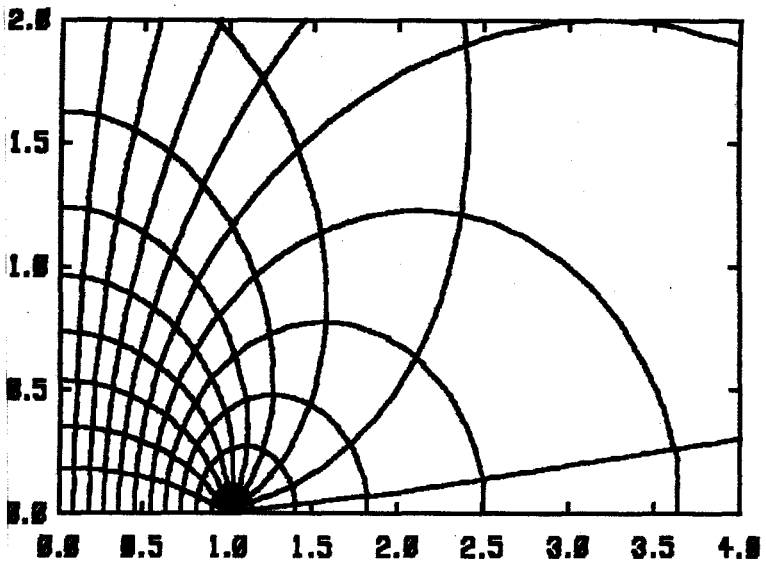

FIGURE 3. B-lines and Equipotentials from a Current Loop.

compressive force. On the outboard side the two forces tend to cancel. This is a principal source of the poloidal asymmetry observed. The source field also has a hoop force effect on the shell current. Early in the disruption when the currents are peaked on the inside, the source current draws the shell outward (and the source current is itself drawn inward).

3. Vertical Field Interaction

The vertical field interaction with the shell current yields a force directed toward the torus major axis, opposite to the hoop force. Depending on the geometry, field strength, and time during the transient, the three forces become more or less dominant. The result is that in some cases there is substantial poloidal variation of the forces but in other cases there is little variation. The magnitude of the vertical field is the primary cause for differences in the time evolution of the loading for different geometries. In some cases the forces are radially inward throughout most of the disruption time and in other cases the inboard side forces are radially outward. The details will be made clearer in the comparative study in Section 5.

Since the vertical field interaction scales as I and the other two forces as I^2, at low values of current the vertical field interaction is the dominant force. This is true at the beginning and end of the structural current transient. This implies that near the end of the current transient when the first wall is most likely to exhibit melting at the surface, the forces tend to be directed toward the major axis. In some designs, the time at which the forces turn inward are very late in the disruption, perhaps even after the plasma current has completely vanished.

1.2. Overview of Stresses

After the pressure loading is known, the response of the shell can be solved. Although it is substantially more complicated, the structural response of the first wall has a general behavior which can also be summarized qualitatively. One of the most interesting aspects of the stress problem in toroidal shells is the existence of "singular points". These points are mathematically singular only when the linear membrane theory is used. The internal forces (the stress resultants) produce

displacements which result in a discontinuous structure. This occurs even for the case of a uniform pressure loading.

The source of incompatibility between the displacements and the original continuous structure can be visualized by considering the two stress resultants acting on the equilibrium, N_θ and N_ϕ. Due to the toroidal symmetry, N_θ has a net component only in the r-direction, or towards the major axis. N_ϕ always acts in the direction tangent to the shell. At the top and bottom, both of these forces point in the same direction. Consequently there is no way for the shell to constrain vertical displacement. The result is a discontinuity at these two points. Allowing non-linear response (i.e. solving the equations at the deformed points) or allowing bending moments and shears will cure this problem. The method adopted here is a complete bending theory solution accounting correctly for the generated moments and shears.

Another feature of the structural problem results from the competition between major and minor radii effects. In the pressure loaded problem the inboard side tends to displace less since the two effects balance, whereas on the outboard side they tend to add. Strains are moderated there somewhat due to the 1/r major radius dependence

$$r\epsilon_\theta = v\cos\phi + w\sin\phi \tag{1}$$

In the eddy current loaded problem, the pressures are inward toward the minor axis and displacements are greater on the inboard side.

The pressurized torus example was used to verify the structural part of the calculation. The commercial Finite Element code PAFEC was used with 3-noded axisymmetric thin shell elements[5]. The results are not presented here, but in general the agreement was within ~5–10%. In all likelihood, the PAFEC calculation was less accurate since so many fewer elements were used. Figs. 4 and 5 display the deformed shell due to uniform pressure loading of 1 Pa. High moments correspond to areas of high curvature. In the figures, the major axis is located off the plot, beneath the x-axis. This is rotated 90° from the usual way of drawing a torus. The quantities in the plot are scaled so that they appear readable.

For example, a displacement off of the undisturbed shell of 1 m in Fig. 4 actually represents 4.8×10^{-8} m.

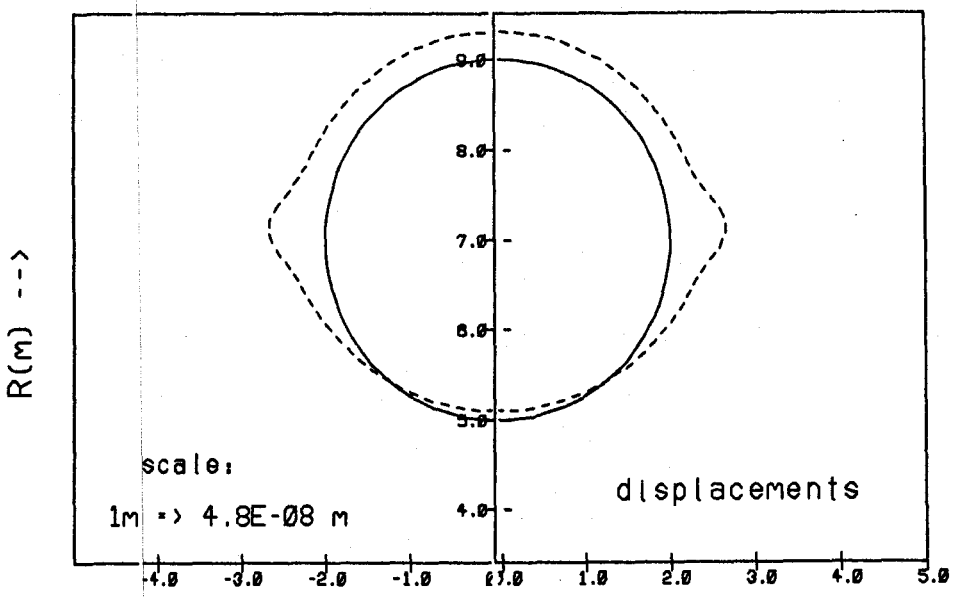

FIGURE 4. Pressurized Torus Displacements.

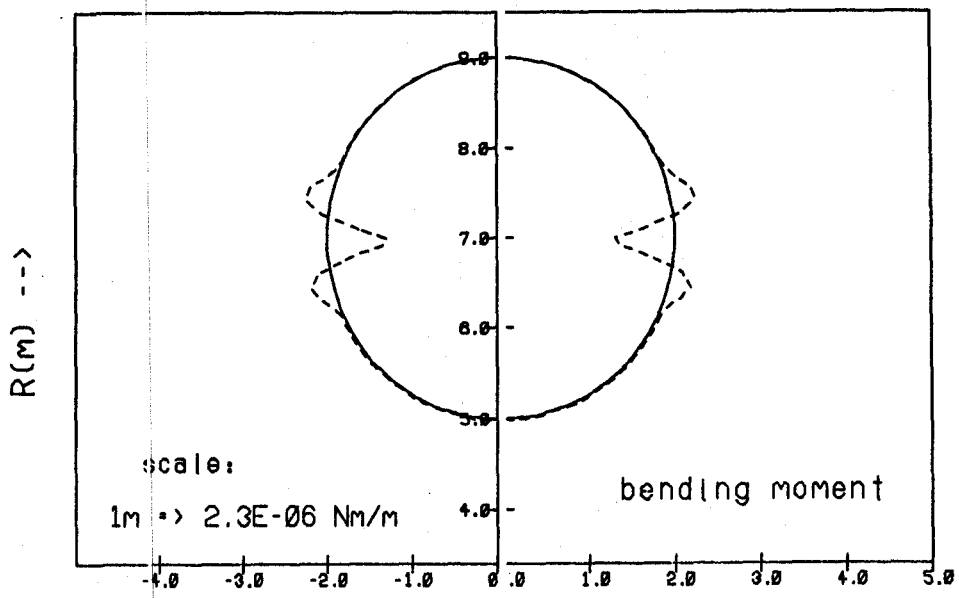

FIGURE 5. Pressurized Torus Moments

2. Description of Computational Method

There are several steps required to compute currents, pressures, and finally strains. Broadly, they can be grouped into two problems: the eddy current problem (including calculation of J $\times$ B forces) and the structural problem.

2.1. The Eddy Current Problem

The eddy current problem is solved using an electric circuit analog. The structure is broken into a large (typically $\sim$100) number of filamentary loops concentric with the source current. Each loop has a resistance, R, and self-inductance, L, associated with it. (See p. 6 for nomenclature.)

$$R = \frac{\eta 2\pi r}{ha\Delta\phi} \tag{2}$$

$$L = \frac{\mu_o}{2\pi}(ln\frac{8r}{b} - 1.75) \tag{3}$$

$$b = \sqrt{ha\Delta\phi/\pi}\ . \tag{4}$$

In addition, each loop couples with the source current and each of the other loops through a mutual inductance. This mutual inductance is computed using the vector potential A_ϕ. The vector potential and the fields, B_r and B_z, used to compute forces are given analytically in terms of complete elliptic integrals E(k) and K(k). The expressions are found in Appendix A. The relationship between the distributed quantity A_ϕ and the discrete mutual inductance is derived from

$$V = \int \mathrm{E}\cdot\mathrm{dl} \tag{5}$$

Substituting the expressions

$$V = M\frac{dI}{dt} \tag{6}$$

and

$$\int \mathrm{E}\cdot\mathrm{dl} = 2\pi r\frac{dA}{dt} \tag{7}$$

we arrive at

$$M = 2\pi r \tilde{A} \tag{8}$$

where $\tilde{A}$ is the vector potential per unit source current.

One of the great simplifications involved in this 1-D model is the absence of "mutual resistances". In a 2-D model where currents are broken into a mesh of loops, bordering loops must share line elements. This feature is absent in the 1-D analysis where each loop has a resistive voltage drop which only depends upon its own current.

These equations are approximations that treat the loops as having circular cross sections with the same cross sectional area as the shell element they model. For the approximation to be valid, there should be enough loops such that $h/(a\Delta\phi)$ is not "too small". In order to avoid a rigorous treatment of this problem, we make the observation that the order of accuracy of the problem is limited but can be improved by increasing the number of loops chosen. The maximum number of loops is limited by storage and execution time which scale as N^2. The worst problems occur when two shells are placed close together. Small scale perturbations (bumpiness) can dominate the response in this case.

The solution of the equations as a function of time is accomplished with a simple explicit differencing scheme. Vector notation (underlining in this case) is introduced wherein the vectors represent columns of values such that each loop contributes one element in the vector. The mutual inductance matrix, $\underline{\underline{M}}$, relates each loop to every other loop, with self-inductances appearing on the diagonal. The matrix circuit equation

$$\underline{\underline{M}} \cdot \frac{d\mathrm{I}}{dt} + R\mathrm{I} + \mathrm{M}_o \frac{dI_o}{dt} = 0 \tag{9}$$

is rewritten in two parts

$$\mathrm{A} = \underline{\underline{M}} \cdot \mathrm{I} + \mathrm{M}_o I_o \tag{10}$$

$$\frac{\eta}{\pi b^2}\mathrm{I} = -\frac{d\mathrm{A}}{dt} \tag{11}$$

The factor $2\pi r$ has been absorbed into $\underline{\underline{M}}$.

The difference equations are:

$$\frac{dA_i}{dt} = \frac{A_{i+1} - A_i}{\Delta t} \tag{11}$$

$$A_{i+1} = A_i - \Delta t \frac{\eta}{\pi b^2} I_i \tag{12}$$

$$I_{i+1} = \underline{\underline{M}}^{-1} \cdot (A_{i+1} - I_o(t) M_o) \tag{13}$$

where the subscript i is a time step identifier. After the currents are known at each time step, the fields due to these currents are computed using the elliptic integral representations given in Appendix A. The pressure loading is a simple cross product

$$p = K \times B \tag{14}$$

$$K = hJ = (I/a\Delta\phi)\hat{\theta} \tag{15}$$

$$p_r = p_R \cos\phi + p_z \sin\phi \tag{16}$$

$$p_\phi = p_z \cos\phi - p_R \sin\phi \tag{17}$$

The entire solution for 1000 time steps and 100 loops typically takes less than 30 seconds on a VAX 11/780. Including plotting of the results, interactive execution and data analysis requires times of the order of minutes.

2.2. The Structural Problem

The structural part of the problem takes the pressures as input and then at any given time step computes the quasi-static structural response in terms of the displacements, strains, shears, moments, etc. The elimination of the inertial terms in the equilibrium equations is not strictly valid. A full time-dependent problem would be easy to implement, but would require orders of magnitude

more computer time. The quasi-static assumption is probably conservative, since at early times when the forces and time derivatives are largest, the inertia tends to decrease the displacements. A dimensionless frequency parameter, Ω, is defined by

$$\Omega = \frac{\omega r}{c} \tag{12}$$

where c, the speed of sound in the material, is given by

$$c = \sqrt{E/\rho} \tag{13}$$

In steel, c is $\sim$ 5 km/s. Hence, for scale lengths on the order of 5 m (and accounting for the factor 2π), the transition to a time-dependent problem should take place at characteristic times (1/f) of $\sim$ 10 msec. This is very close to the 25 msec used in the following analysis. The derivation of the static equations is given in Appendix B, and follows closely the work of Flugge[6] and Timoshenko[7].

Note that the limitation on the pressure data due to the N^2 nature of the eddy current problem is not a factor here since the structural problem has storage and execution time scaling as N (where N is the number of elements). The pressure data is therefore interpolated using cubic B-spline interpolating functions. As many as 1000 points are typically used in the structural problem. This greatly improves the accuracy of the structural problem which is limited by constant element size.

A finite element method (FEM) is employed in order to convert the set of coupled partial differential equations into a matrix of algebraic equations which requires only one large matrix inversion for their solution. For a one-dimensional problem broken into N elements with M unknowns to be solved at each point, the matrix is NxNxMxM. With pentic spline basis functions, each equation involves only five points, therefore the matrix rows contain only 5 blocks each with full MxM blocks. Most of the matrix is filled with zeros. By using a special purpose block penta-diagonal banded matrix system solver, a tremendous savings in time and storage is made. Whereas the execution time of a full matrix inverter scales as N^2, the penta-diagonal system scales as N.

The B-spline basis functions $B_i(\phi)$ used in the FEM analysis are described in detail in Appendix C and plotted in Fig 6. As far as the equations are concerned,

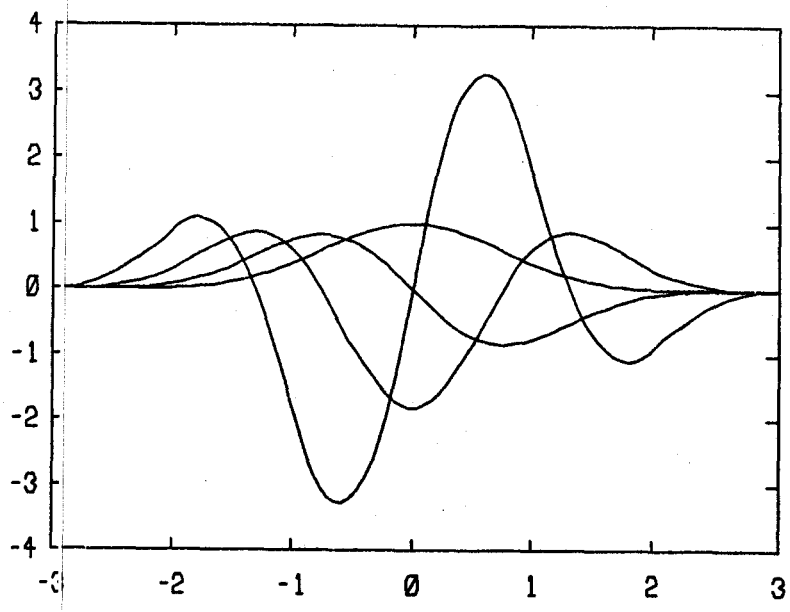

B-Spline Basis Function and Derivatives

FIGURE 6.

B-splines are simply 5th order polynomials. Mathamatically, they must result in the same solution as any 5th order polynomial. The primary reason for using them is their simplicity and ease of application, resulting mainly from the absence of the explicit occurrence of matching conditions at the element boundaries.

5th order B-splines were not the original choice of basis functions. Cubic B-splines were attempted, but the discontinuity in their third derivative resulted in the solution being dependent on the number of nodes, particularly for the moments which enter the equations as the highest derivative of the displacements. By approximating the third derivative as the average value at the discontinuity, accurate displacements were obtained, but moments and shears were not consistant. Inspection of the structural equations reveals that even the 4th derivative enters into the moment equations.

The four unknown quantities are approximated in terms of the basis functions (using the summation convention) as follows:

$$u(\phi) = \sum_i \alpha_i B_i(\phi) \equiv \alpha_i B_i(\phi) \tag{18}$$

$$v(\phi) = \beta_i B_i(\phi) \tag{19}$$

$$Q_\phi(\phi) = \gamma_i B_i(\phi) \tag{20}$$

$$M_\phi(\phi) = \delta_i B_i(\phi) \tag{21}$$

The sums contain only five terms since B_i is zero except for

$$(\phi_i - 3\Delta\phi) < \phi < (\phi_i + 3\Delta\phi) \tag{22}$$

At each point for each of the unknowns the splines B_i are evaluated and the contributions of the neighbors are added in

$$u(\phi_i) = u_i = \alpha_{i+2} + 26\alpha_{i+1} + 66\alpha_i + 26\alpha_{i-1} + \alpha_{i-2} \tag{23}$$

Similarly for the derivatives,

$$u'(\phi_i) = u'_i = 5\alpha_{i+2} + 50\alpha_{i+1} - 50\alpha_{i-1} - 5\alpha_{i-2} \tag{24}$$

$$u''(\phi_i) = u''_i = 20\alpha_{i-2} + 40\alpha_{i-1} - 120\alpha_i + 40\alpha_{i+1} + 20\alpha_{i+2} \tag{25}$$

These forms are substituted into the reduced set of structural equations, which results in four equations (one for each j) at each point x_k

$$A_{ij}(x_k)\alpha_i + B_{ij}(x_k)\beta_i + C_{ij}(x_k)\gamma_i + D_{ij}(x_k)\delta_i = p_j \tag{26}$$

where p_j contains the terms with the externally applied pressure and the i sums range only from $k - 2 < i < k + 2$ since the splines are zero elsewhere. A, B, C, and D contain all of the information from evaluating the coefficients of the structural equations at each point. We can also write a more general form,

redefining A and replacing the four equations with

$$A_{ijl}\alpha_{il} = p_j \tag{27}$$

The l index ranges through the 4 equations. The entire system of equations can now be expressed as one matrix equation

$$A_{ijkl}\alpha_{il} = p_{jk} \tag{28}$$

where α_{il} is the generalized N by 4 spline coefficient matrix, and i and k are point indices and j and l are equation indices. A_{ijkl} is a block penta-diagonal matrix. It has 5 full 4x4 blocks in each row which contain the equation information at a given point and its four nearest neighbors.

3. Base Case

3.1. Description of Base Case

There is a large number of examples which could be studied. The quantities in a reactor design which affect the calculation are: a, R, I(t), B_v, η, h, E, and ν. Each unique choice of these variables results in a different loading and structural response. In order to limit the number of cases studied and also to include reactor-relevant examples, a base case design was chosen using data from the STARFIRE reactor design[2]. The STARFIRE structure is far too complex to model in detail using only this 1-D model. For the purposes of this calculation, the details of the first wall and blanket region are homogenized such that the structure becomes a simple circular cross section, constant thickness, constant resistivity shell. Some of the numbers are included in Table 1 (section 5).

In addition to these, the material properties and wall thickness must be lumped into single numbers. STARFIRE employs a two-layer first wall of 1.5 mm austentitic stainless steel coated with 1.0 mm beryllium. The steel is responsible for the majority of the structural stiffnes, whereas the beryllium provides the majority of the electrical conductivity. Most of the forces are generated in the Be coating and supported structurally by the steel. We will consider the average properties of the wall, although it is certainly possible that the coating could detach from the steel during disruption, in which case the forces would not transfer to the steel and consequences would be much more severe. The following parameters are obtained by averaging the properties of the two materials, weighted by their thickness:

$$\eta = 5.54\,\mu\Omega - \text{cm}$$
$$h = 1.5\,\text{mm}$$
$$E = 190\,\text{GPa}$$
$$\nu = 0.3$$

Throughout the comparative study these quantities remain fixed.

In STARFIRE, conducting paths behind the first wall account for the equivalent of $\sim$ 2 cm of stainless steel. In the comparative study, this outer shell was

not included. Instead, a special case was studied comparing the base case with and without a second conducting shell, also called an electromagnetic shield.

3.2. Base Case Results

Each of the cases studied in this report was modeled with 48 element loops, except for the two-shell case. An exponential plasma decay time was fixed at 25 msec. In the STARFIRE design, this time constant was varied between zero and 400 msec for the analysis of electromagnetic effects (section 10.7 of Ref. 2). In the ETF/INTOR study, 25 msec was used. The actual time evolution of a plasma disruption is actually more complicated than a simple exponential. There are thought to be different time constants associated with the thermal energy deposition and the current decay. For the current decay, there is probably a phase during which the currents redistribute before they actually disappear. This study adopts the INTOR value with the understanding that the current decay time is an important parameter which is relatively unknown.

Referring to the time histories (Figs. 7 and 8), it can be seen that the structural response time is approximately 100 msec. This is sufficiently longer than the 25 msec transient time constant such that the profiles can be considered to contain two regimes: the ramp up to peak currents at $\sim$ 30 msec and the structural decay. The largest pressures and strains occur after the ramp-up and are relatively independent of the details of the magnetic diffusion and ramp-down.

The peak current varies between 120 – 140 kamps from outboard to inboard loops. The total current transferred is therefore approximately 6.25 MAmps out of 10 MA plasma current. This is entirely due to the ratio of mutual to self inductance of the shell, since there hasn't been time enough for resistive decay to act.

Referring now to the spatial profile of the induced current (Fig. 9), it can be seen that the poloidal asymmetry is small and decreases with time. Initially only current in the inboard part of the torus maintains the central flux. After the field diffuses into the torus, the current flattens.

The pressures show a much greater poloidal asymmetry than the currents (Figs. 10-11). This is due to the I^2 dependence of forces as well as the $1/r$ field dependences. An interesting feature is the change in shape as a function of time. At first, all of the pressures are radially inward, peaked near the major axis. Later, as the vertical field interaction takes over, the inboard pressure passes through zero and at large times is radially outward.

The circumferential (phi-directed) pressures are down approximately a factor of 10 from the radial pressures. Some of the unexpected behavior in the displacement and bending plots can be explained by these. Early in the disruption there is a force toward the top and bottom points. Later, the $\sin\phi$ dependence indicates an inward force toward the axis due to B_v.

The displacement plots for the base case (Fig. 12) show the combined influence of the pressure loading (both radial and circumferential) as well as the tendency for the rotations to be supported at the top and bottom points. The strains do not show the same peaking as the moments and displacements. Initially there is a net outward motion of 2–3 mm with an accompanying minor radius compression of 1–2 mm. Peak strain levels are $\sim 5 \times 10^{-4}$ poloidal strain and $\sim 1.5 \times 10^{-4}$ toroidal strain, both occuring at the inboard edge. These levels are not likely to destroy the structure immediately unless stress concentrations occur near discontinuities. However, they are not insignificant from the point of view of impact on lifetime due to fatigue when other sources of wall damage are considered.

Later in the disruption the strains drop and the structure moves toward the axis. Since the computational method does not include time dependence in the structural equations, the recoil effect is unknown. This will add to the strains at later times, but these are not the largest ones, so the quasi-static solution is probably still conservative. More plots of moments and strains appear in the following section.

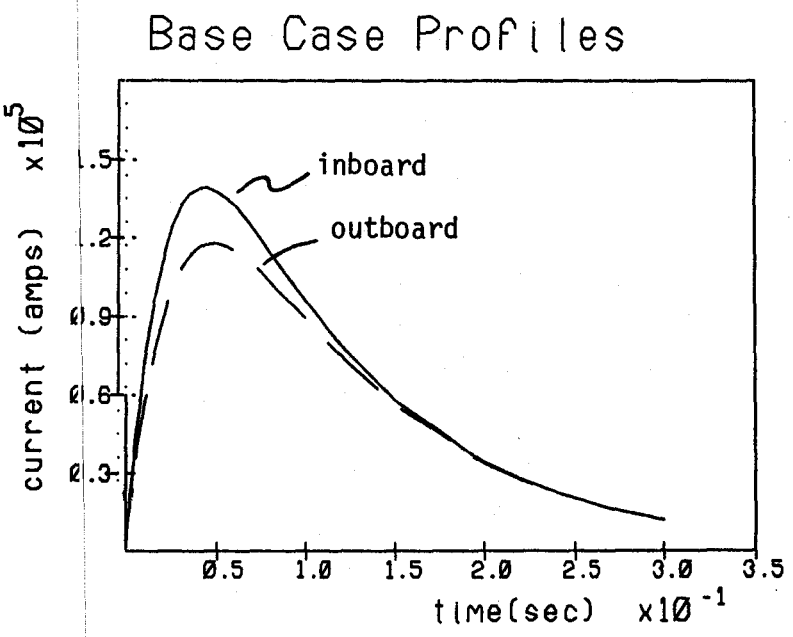

FIGURE 7

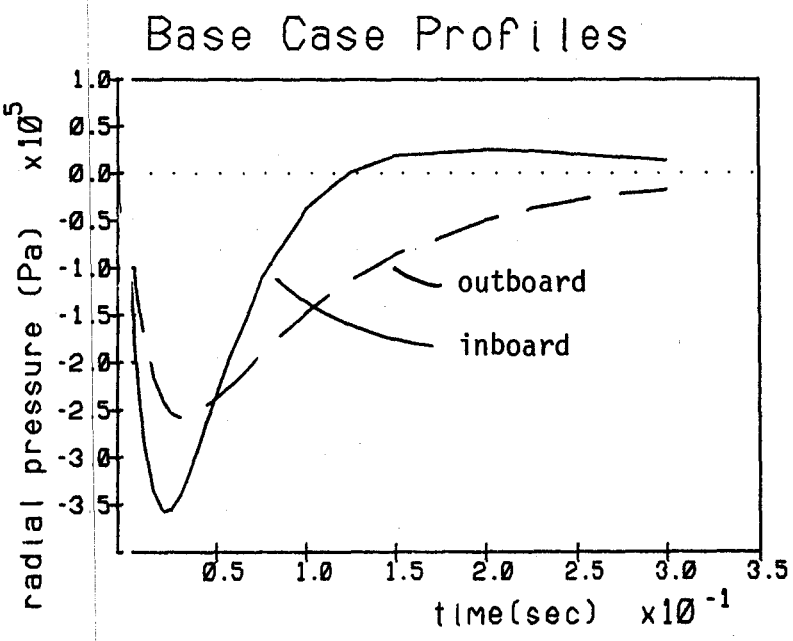

FIGURE 8

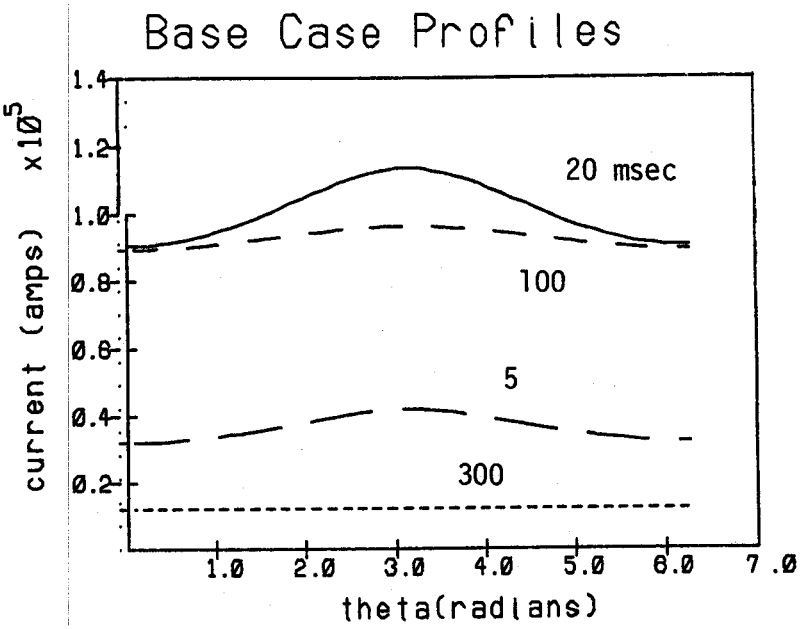

FIGURE 9

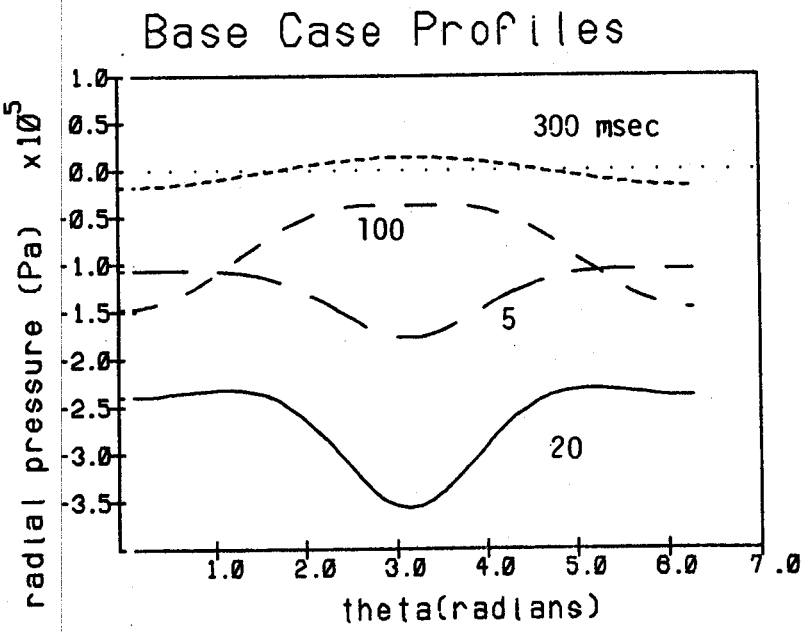

FIGURE 10

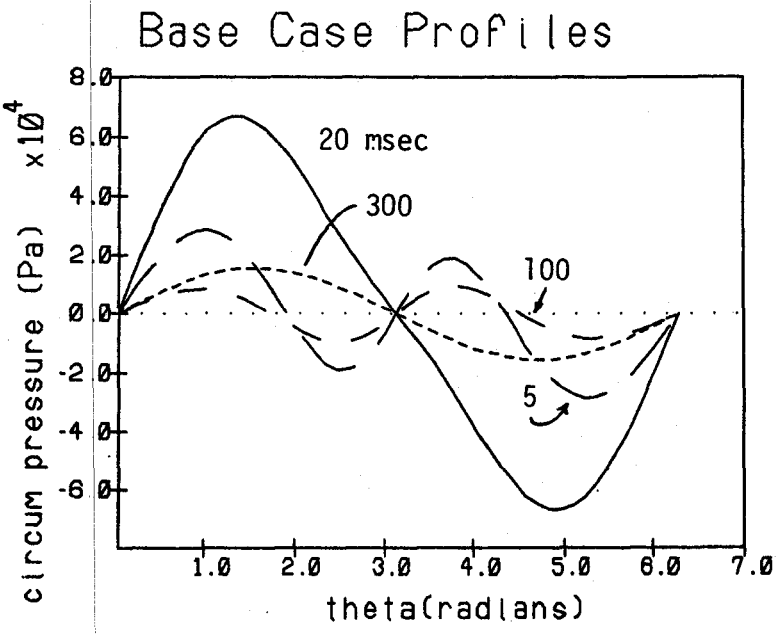
Base Case Profiles
circum pressure (Pa) x10^4
8.0
6.0
4.0
2.0
0.0
-2.0
-4.0
-6.0
20 msec
300
100
5
1.0
2.0
3.0
4.0
5.0
6.0
7.0
theta(radians)

FIGURE 11

Base Case Displacements

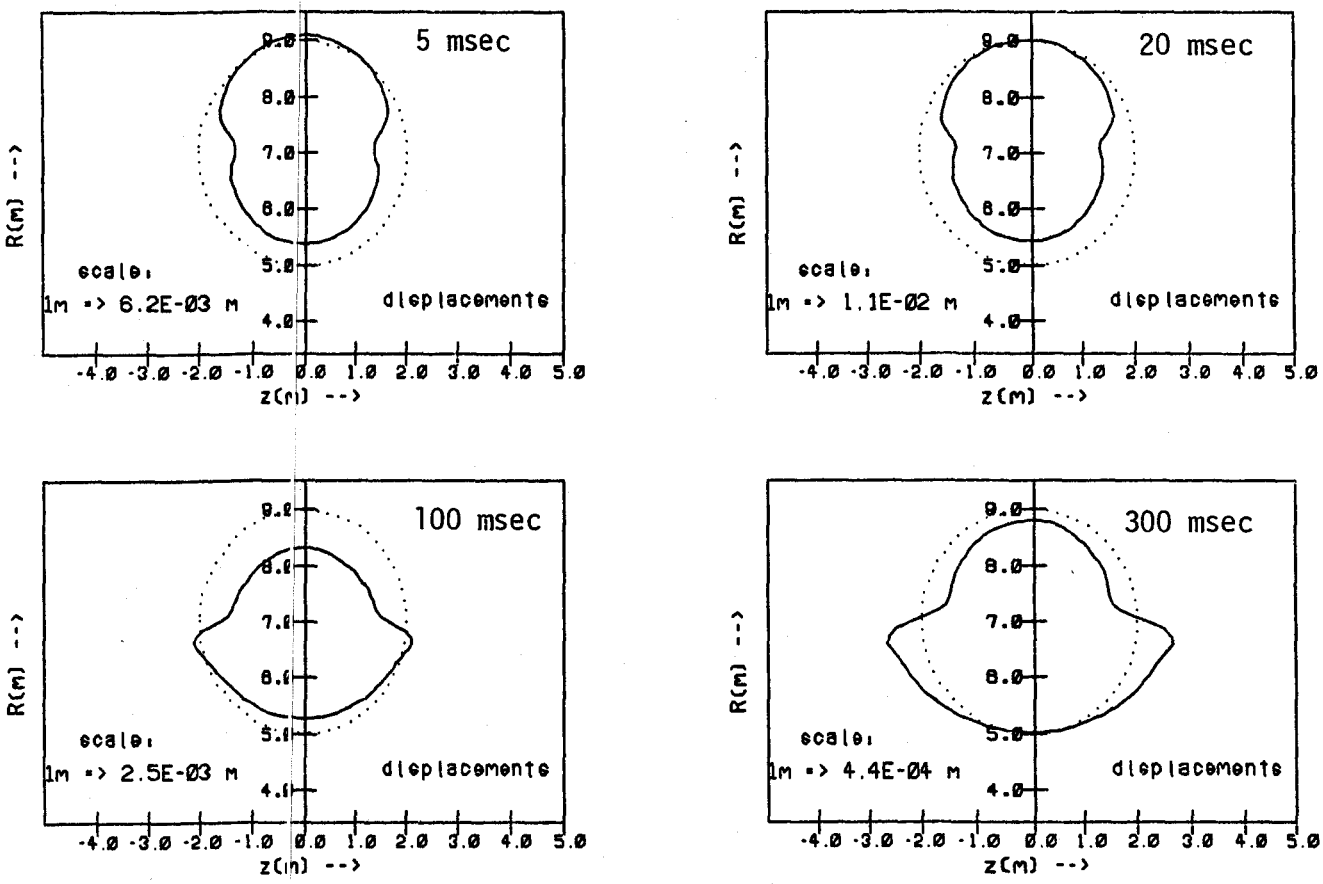

FIGURE 12

4. Variation of Parameters

There are two possible ways to vary the important parameters in this problem. One could leave all of them constant except one and then examine the effect of independently varying that one. In this study, it was decided that a more enlightening method requires that all of the tokamak parameters vary together in a self-consistent fashion. The total reactor power output is fixed at the base case value as is the rotational transform at the limiter. This leads to 5 constraint equations and 8 unknowns, leaving 3 free parameters which can be varied independently.

4.1. Equations Used for Self-Consistency

The 8 unknowns are: a, R, I, B_t, B_p, B_v, $\langle\beta_t\rangle$, and $\langle\beta_p\rangle$. The reactor power output for a given temperature and q(a) are given by,

$$W \sim \left\langle \beta_t^2 \right\rangle B_t^4 a^2 R \tag{29}$$

$$q_a = \frac{2\pi a^2 B_t}{\mu_o R I} \, . \tag{30}$$

In addition, the two defining equations for B_p and β_p are:

$$B_p = \frac{\mu_o I}{2\pi r} \tag{31}$$

$$\frac{\beta_p}{\beta_t} = \frac{B_t^2}{B_p^2} \, . \tag{32}$$

Finally, the vertical field equilibrium is given by,

$$\frac{B_v}{B_p} = \frac{a}{2R}(ln\frac{8R}{a} + \langle\beta_p\rangle - 2.25) \, . \tag{33}$$

The three free parameters are then $\langle\beta_t\rangle$, B_t, and a/R. Each is varied while keeping the other two fixed to the base case value. In Table 1, the four cases are summarized.

Table 1 — Data for Comparative Analysis

A STARFIRE-like base case
B low β – giving higher current, lower B_v, and larger dimensions
C high aspect ratio – giving lower current and higher B_v
D high field – giving larger B_v and smaller dimensions

(all magnetic fields are measured on axis)

Parameters for the 4 Cases Studied				
	A	B	C	D
minor radius a [m]	2	2.82	1.78	1.24
major radius R [m]	7	9.87	8.88	4.35
plasma current I [MA]	10.1	14.1	6.3	8.96
toroidal field B_t [T]	7	7	7	10
poloidal field $B_p(a)$ [T]	0.35	0.25	0.39	0.50
vertical field B_v [T]	.067	0.04	.067	.067
toroidal beta $\langle\beta_t\rangle$	2.91	1.74	4.16	2.90
poloidal beta $\langle\beta_p\rangle$	1.0	1.0	0.7	1.43

4.2. Results From Variation of Parameters

Appendix D contains plots of the results. The induced current profiles from the 4 cases show few significant differences (Figs. D.1 and D.2). The magnitudes of the induced currents simply reflect the magnitude of the driving currents. The flatness of the profiles is mostly a function of aspect ratio with some dependence on absolute size because of the difference in structural time constants. Based solely on the induced currents, one would choose the design with the lowest plasma current – case C.

The pressure profiles show more marked differences (Figs. D.3–D.5). Part of this is due to the I^2 dependence, but notice also that the compact machine,

case D, has a large poloidal asymmetry and much larger forces due to the larger external fields present. At later times (> 100 msec) the four induced current profiles have already peaked and returned to levels comparable to the 20 msec profiles. However, the driving current has dropped significantly, leading to much altered pressure profiles. At 100 msec, the four pressure profiles have approached one another in both shape and magnitude. The low β machine (case B), with lower B_v shows the least tendency for a radially outward pressure until very late in the disruption. Based on the radial pressures, the high aspect ratio machine has the most desireable response and the high field case has the worst.

The peak strains for all cases range between 5 and 10×10^{-4}, except for the high aspect ratio case (Figs. D.6–D.13). It peaks at under 10^{-4} and also shows the least poloidal variation early in the disruption. The other 3 cases show few remarkable differences. The strain profiles exhibit much less variation than the displacement plots. The primary difference is in the relative magnitudes. The high field case is clearly the worst, with peak strains of 10^{-3} and peak bending stresses of 1.8 MPa (18 atm).

4.3. Effect of Large Plasma Shift

The plots of field lines and field contours are very revealing when discussing the effect of plasma shift. A circular shell centered at the current loop sees a larger field at its inboard edge compared to outboard. But a correct amount of shift of the central current with respect to the shield would nearly align the shell with the field lines. This amount of shift is the same order of magnitude as the shift expected in a normal high beta equilibrium.

The equipotential lines are the same lines along which forces act, since they are perpendicular to both I and B_v. This explains why most of the pressure is directed radially.

This test case has all of the input parameters of the base case, except the 10 MA driving current was shifted out 50 cm. The results show that the amount of shift was slightly greater than that needed to flatten the profiles. The inboard radial pressure has flipped around so that it is always more positive than the outboard

side. Peak pressures are larger because the driving current is now closer to the shell. This increases the mutual inductance as well as the field seen at the shell. At later times, the structure's natural electrical response dominates and the profile is almost indistinguishable from the case with a central current.

4.4. Effects of an Electromagnetic Shield

The test case with an electromagnetic shield was intended to model the STARFIRE conducting blanket region. For plasma stability, at least 2 cm equivalent stainless steel is said to be required. This number was used, with the radial position of the shield at 10 cm behind the first wall. A large number of loops (200) was used for this case because of the close spacing between the first and second shells. Spacings closer than 10 cm required too many loops for the desired degree of accuracy. Even so, some small scale non-uniformity is apparent in the structural plots, especially in the moment plot.

The first conclusion from the results is that the shape of the pressure profiles is relatively unchanged. The magnitude is down by about a factor of two; at 20 msec the peak values are .35 and .17 MPa (Figs. 10 and 14). The effective structural time constant is lengthened by the presence of the shield. In this example the conductance of the shield is approximately equal to that of the first wall due to the much lower conductivity of stainless steel compared to beryllium ($\eta_{ss} = 72\mu\Omega$-cm, $\eta_{be} = 4\mu\Omega$-cm). It is probably safe to assume that a higher conductivity shield would have greater moderating effect on the pressures and hence the stresses.

5. Conclusions

A simple one-dimensional computer model has been developed to compute forces and strains generated in toroidal shells due to eddy currents induced by plasma disruptions. The method uses a circuit analog for computing induced currents and pressures, wherein any toroidal axisymmetric structure can be broken into a set of circular loops with resistances and mutual inductances which are used to form a matrix loop voltage equation. The structural problem involves

calculating stresses and strains by expressing the full set of bending equations in a finite element formulation. In addition to the computer programs, a clear intuitive picture is available for understanding the structural response involving the three basic forces acting on the shell: radial compression, hoop force, and vertical field interaction. For different combinations of the basic reactor parameters, these forces become more or less dominant with respect to one another.

Typical values of pressure (using the base case) ranged from .25 to .35 MPa from the inboard to the outboard sides of the torus. This resulted in a peak displacement of 1 cm, strain of 5×10^{-4}, and bending stress of .7 MPa. Various regimes of reactor parameters studied show that there are significant variations in both the magnitude and spatial profiles of the induced forces. As might have been expected, the design with the largest strain is the high field, low aspect ratio machine. Pressures and strains both increase by a factor of two, whereas the applied current was decreased by 10%.

Plasma shift tends to reduce the poloidal peaking, but in the case studied, the shift was enough to reverse the pressure profiles. This resulted in larger forces, strains, and bending stresses as compared to the base case. The peak pressure occurs at the outboard edge rather than inboard, and peak strains switch from poloidally to toroidally directed.

The technique developed here is very efficient, taking only minutes to execute and analyze a case. This allows for easily examining a wide range of problems. Future improvements suggested include the analysis of forces on magnetic field coils and the ability to model toroidal loops outside the shell, for example a poloidal limiter. Also, a full time-dependent treatment could be implemented using the same programs modified for time integration.

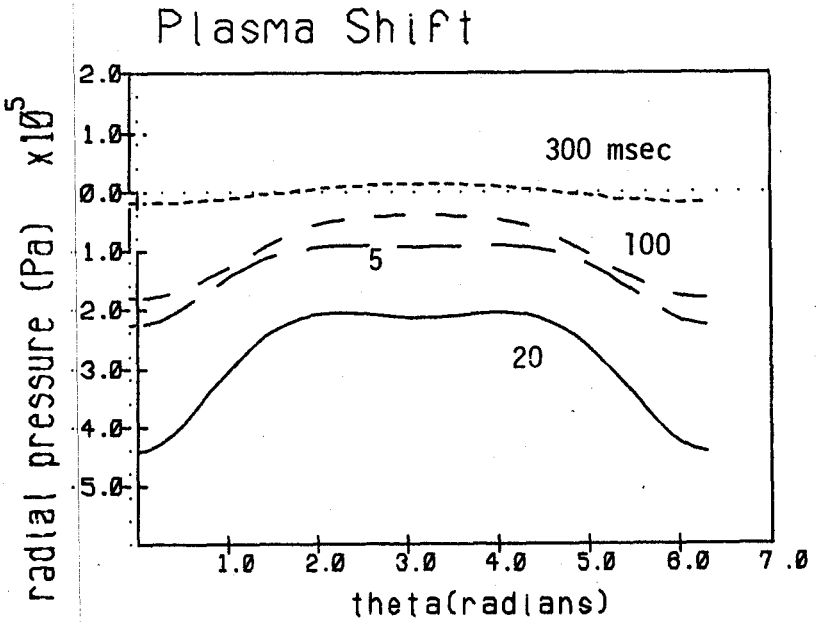

FIGURE 13

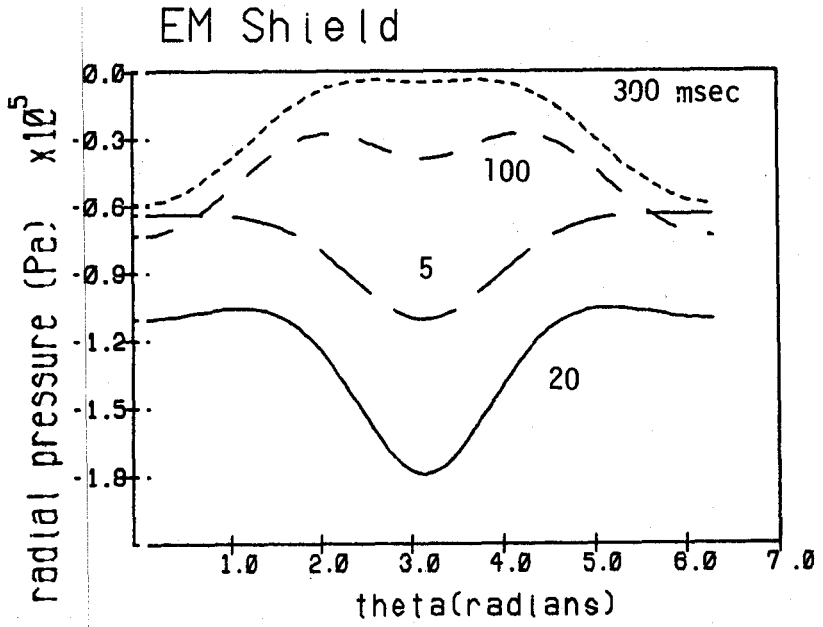

FIGURE 14

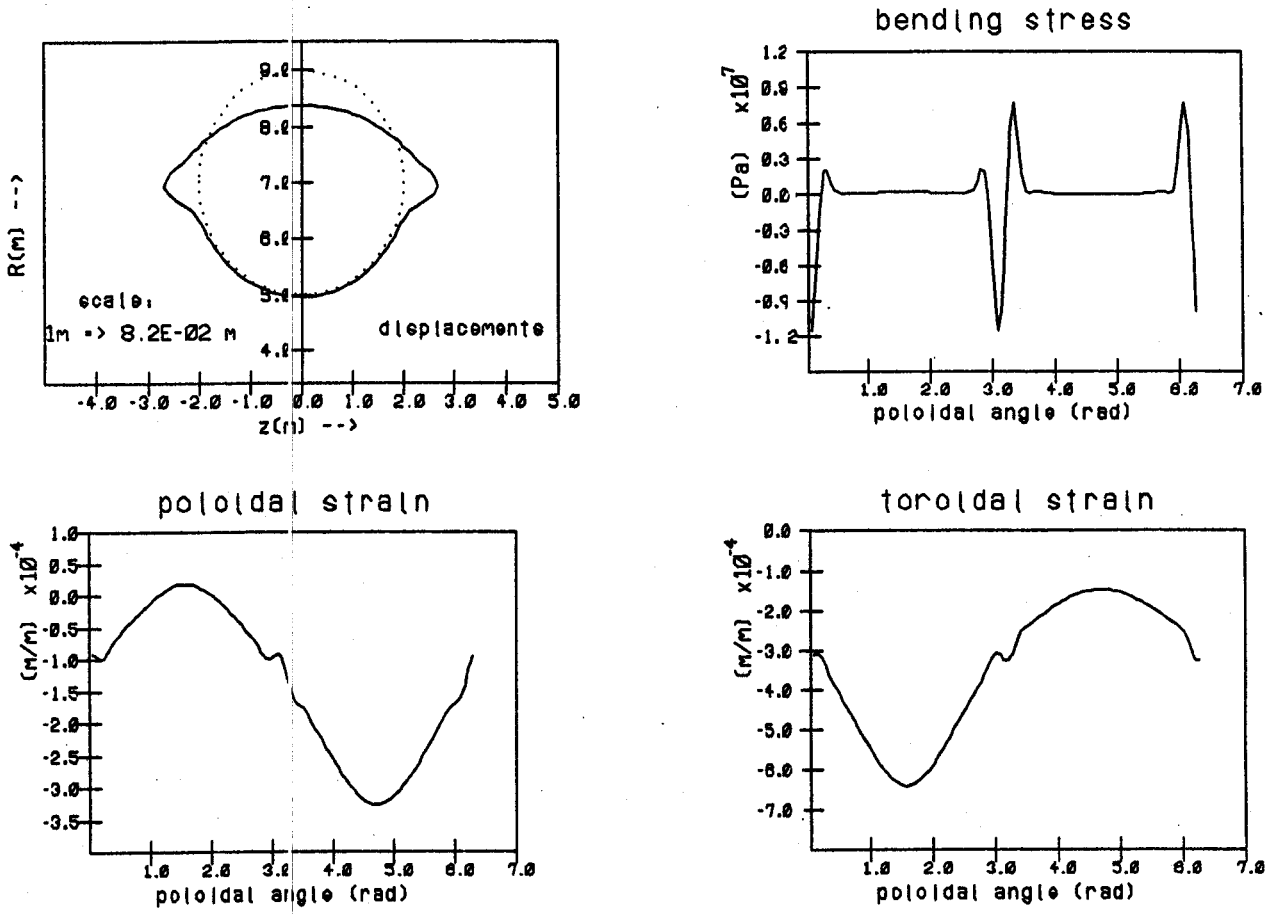

FIGURE 15. Structural Response at 20 msec for Plasma Shift.

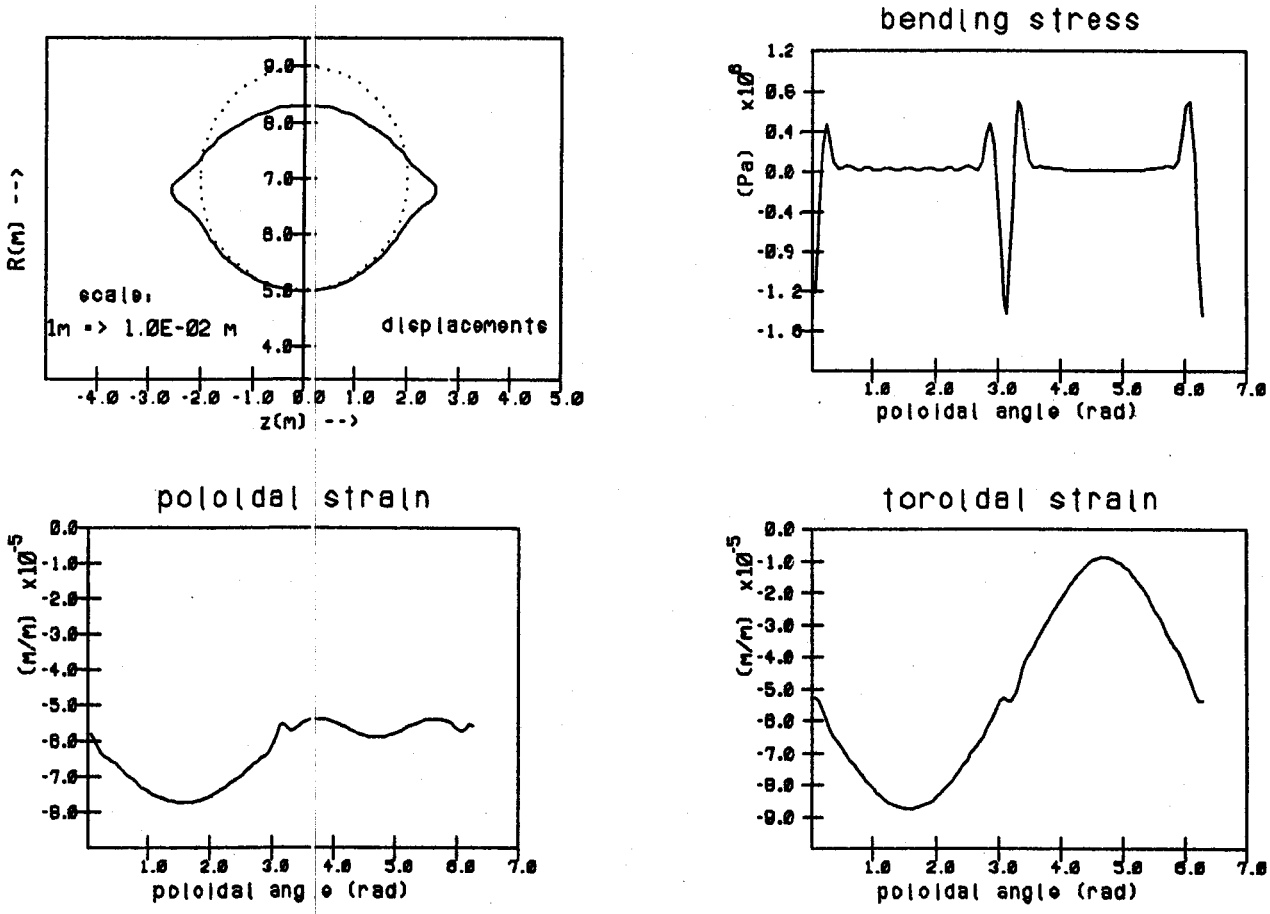

FIGURE 16. Structural Response at 100 msec for Plasma Shift.

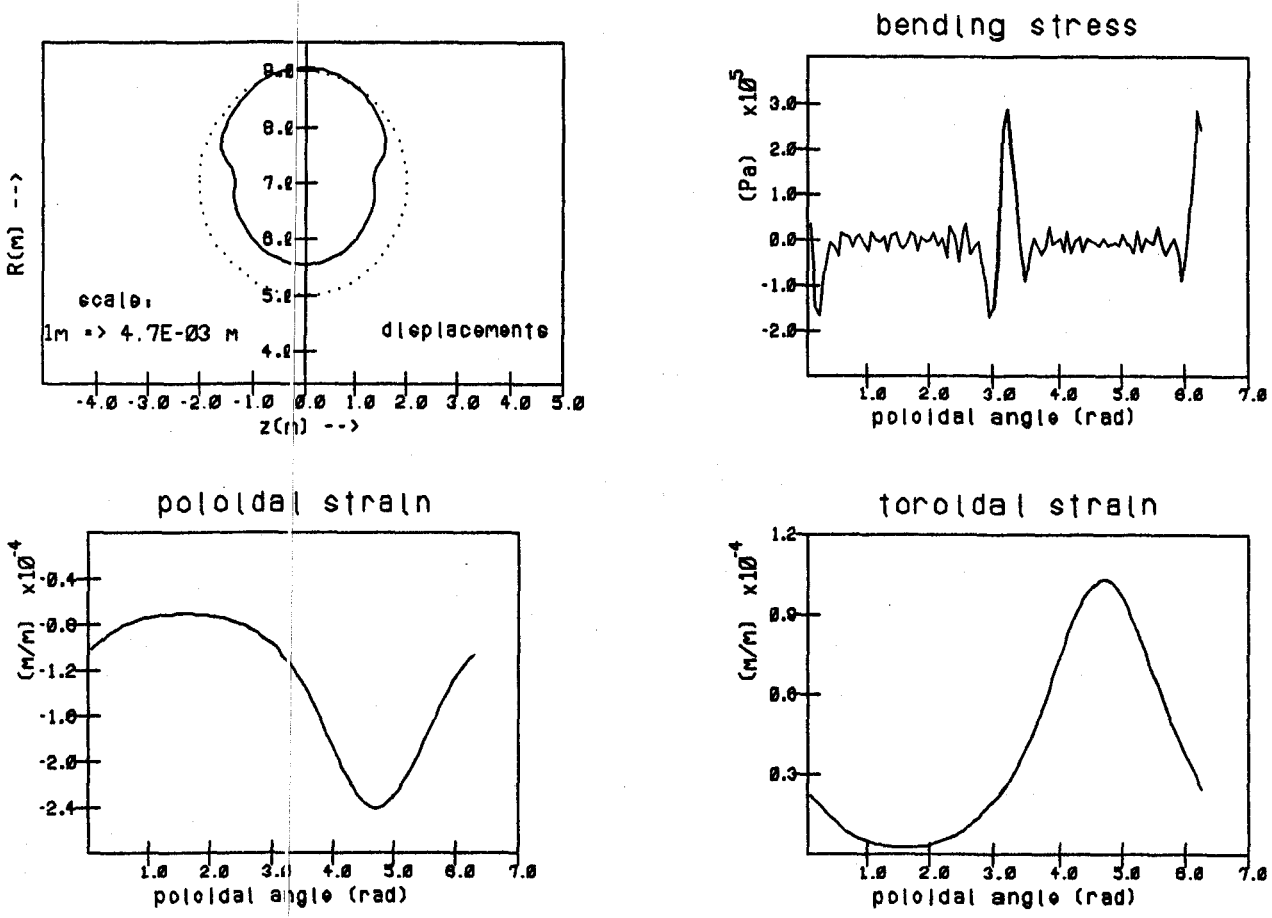

FIGURE 17. Structural Response at 20 msec for EM Shield.

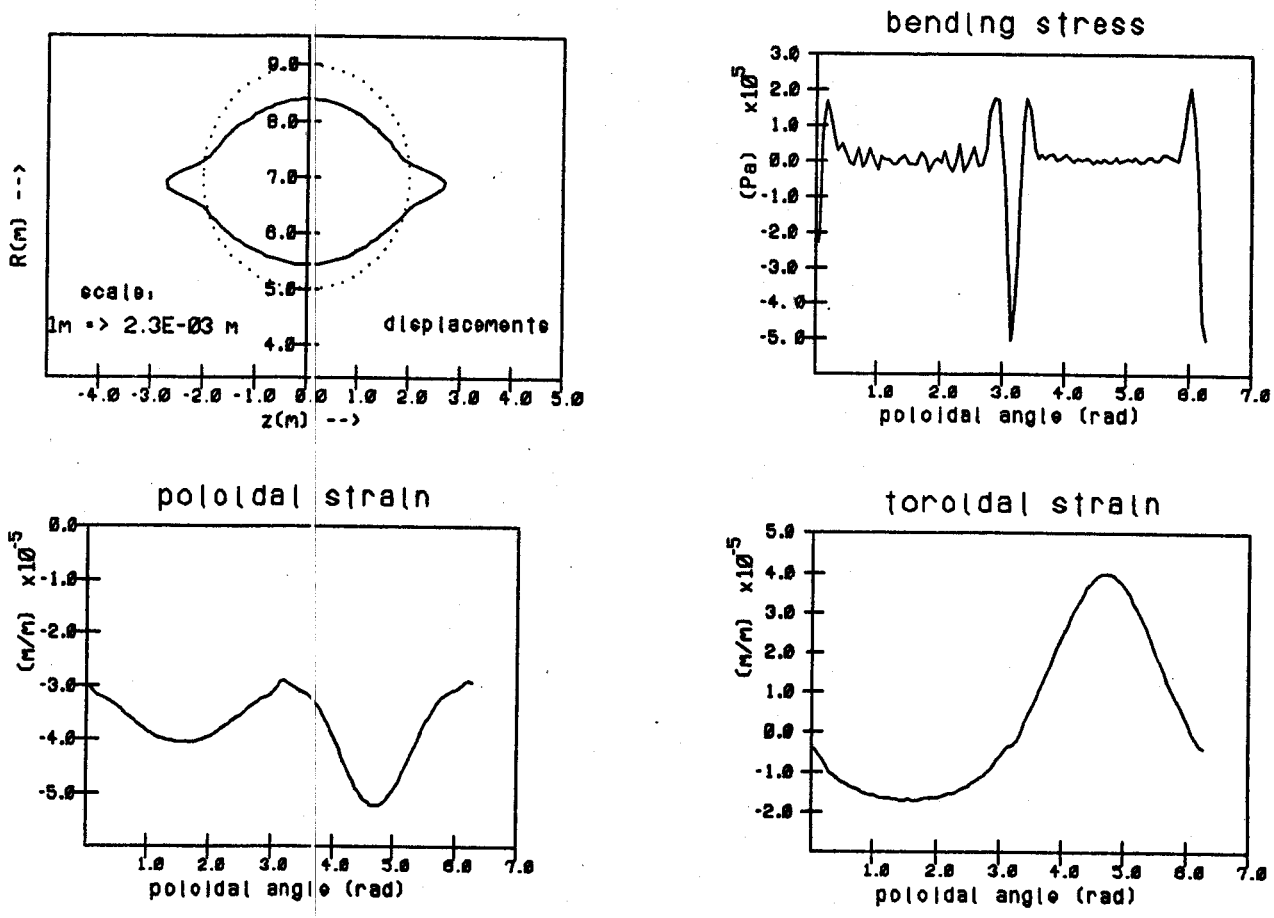

FIGURE 18. Structural Response at 100 msec for EM Shield.

References

1. C. A. Flanagan, D. Steiner, and G. E. Smith, "*Fusion Engineering Device Design Description*," vol. 1, ORNL/TM-7948, 1981.

2. C. C. Baker et al, "STARFIRE – A Commercial Tokamak Fusion Power Plant Study," vols. I and II, ANL/FPP-80-1, 1980.

3. U.S. FED-INTOR Critical Issues, vol. 1, USA FED-INTOR/82-1, 1982.

4. P.H. Sager et al, "FED Baseline Engineering Studies Report," ORNL/FEDC-82/2, April 1983.

5. PAFEC 75 Theory Manual, PAFEC Ltd., Nottingham England, 1976.

6. W. Flugge. Stresses in Shells, Springer-Verlag, New York, 1966.

7. S. Timoshenko and S. Woinowsky-Krieger. Theory of Plates and Shells, Mc-Graw-Hill, New York, 1959.

8. J. D. Jackson. Classical Electrodynamics, John Wiley and Sons, New York, 1975.

Appendices

APPENDIX A — MAGNETIC FIELDS

Field from a Circular Loop

The magnetic field and vector potential due to a circular current loop is well documented in the literature (See Jackson, pp 177-178)[8]. The equations are repeated here for reference.

$$A_\phi = \frac{\mu_o R}{\pi} \frac{(2-k^2)\mathrm{K}(k) - 2\mathrm{E}(k)}{k^2\sqrt{R^2+r^2+2Rr\sin\alpha}} \tag{A.1}$$

$$B_R = \frac{-\mu_o}{4\pi} \frac{2\mathrm{K}(k) - \mathrm{E}(k)\left(\frac{2-k^2}{1-k^2}\right)}{\tan\alpha\sqrt{R^2+r^2+2Rr\sin\alpha}} \tag{A.2}$$

$$B_z = \frac{\mu_o}{4\pi} \frac{2\mathrm{K}(k) - \left(2 - k^2\left(\frac{R+r\sin\alpha}{r\sin\alpha}\right)\right)\mathrm{E}(k)/(1-k^2)}{\sqrt{R^2+r^2+2Rr\sin\alpha}} \tag{A.3}$$

$$k^2 = \frac{4Rr\sin\alpha}{R^2+r^2+2Rr\sin\alpha} \tag{A.4}$$

APPENDIX B — STRUCTURAL EQUATIONS

In the equations that follow, we use the abbreviations for the bending rigidity and flexural rigidity

$$K = \frac{Eh^3}{12(1-\nu^2)} \tag{B.1}$$

$$D = \frac{Eh}{1-\nu^2} \tag{B.2}$$

In addition, by virtue of the somewhat untraditional coordinate system, the radial distance from the axis of symettry is given by

$$R = R_o + a\sin\phi \tag{B.3}$$

Equilibrium Equations

A force balance on the shell element is performed in the phi- and r-directions and a moment balance perpendicular to r and phi, yielding

$$(rN_\phi)' - aN_\theta\cos\phi - rQ_\phi = -arp_\phi \tag{B.4}$$

$$(rQ_\phi)' + aN_\theta\sin\phi + rN_\phi = arp_r \tag{B.5}$$

$$(rM_\phi)' - aM_\theta\cos\phi - arQ_\phi = 0 \tag{B.6}$$

Deformation Relations

Using the strain-displacement relations:

$$a\epsilon_\phi = \frac{dv}{d\phi} + w \tag{B.7}$$

$$r\epsilon_\theta = v\cos\phi + w\sin\phi \tag{B.8}$$

$$a^2\chi_\phi = \frac{d}{d\phi}\left(v - \frac{dw}{d\phi}\right) \tag{B.9}$$

$$ar\chi_\theta = \cos\phi\left(v - \frac{dw}{d\phi}\right) \tag{B.10}$$

and Hooke's law:

$$N_\phi = D(\epsilon_\phi + \nu\epsilon_\theta) \tag{B.11}$$

$$N_\theta = D(\epsilon_\theta + \nu\epsilon_\phi) \tag{B.12}$$

$$M_\phi = -K(\chi_\phi + \nu\chi_\theta) \tag{B.13}$$

$$M_\theta = -K(\chi_\theta + \nu\chi_\phi) \tag{B.14}$$

we derive the deformation relations:

$$N_\phi = D\left[\frac{1}{a}\left(\frac{dv}{d\phi} + w\right) + \frac{\nu}{r}(v\cos\phi + w\sin\phi)\right] \tag{B.15}$$

$$N_\theta = D\left[\frac{1}{r}(v\cos\phi + w\sin\phi) + \frac{\nu}{a}\left(\frac{dv}{d\phi} + w\right)\right] \tag{B.16}$$

$$M_\phi = \frac{K}{a}\left[\frac{d}{d\phi}\left(\frac{1}{a}\frac{dw}{d\phi} - \frac{v}{a}\right) + \frac{\nu\cos\phi}{r}\left(\frac{dw}{d\phi} - v\right)\right] \tag{B.17}$$

$$M_\theta = \frac{K}{a}\left[\frac{\cos\phi}{r}\left(\frac{dw}{d\phi} - v\right) + \nu\frac{d}{d\phi}\left(\frac{1}{a}\frac{dw}{d\phi} - \frac{v}{a}\right)\right] \tag{B.18}$$

These are then solved together with the 3 equilibrium equations, making 7 equations and 7 unknowns. Due to the form of the deformation relations, it is easy to eliminate equations if desired. In the analysis described in this report, M_θ, N_θ, and N_ϕ were eliminated leaving four equations in u, v, Q_ϕ, and M_ϕ. The moment results are expressed in terms of the bending stress which is related through the relation:

$$\sigma_b = \frac{6M_\phi}{h^2} \tag{B.19}$$

APPENDIX C — B-SPLINES AS BASIS FUNCTIONS

B-splines are really just polynomials which can be used like the more standard power series representations for the purpose of fitting data, interpolating pointwise specified functions, and in particular as basis functions for finite element analysis. Like "normal" polynomials such as

$$ax^5 + bx^4 + cx^3 + d^2 + ex + f \ , \qquad (C.1)$$

B-splines have derivatives which are trivial to evaluate. However, B-splines have the very desireable property that functions modeled with them have continuous first and second derivatives throughout the entire domain — including at the nodal points — without the need to add boundary equations on the continuity of these derivatives. In essence, the boundary conditions are incorporated into the basis functions themselves. Another advantage appears in the final matrix equation which must be solved for the displacements. Its form is much simpler since there is only one set of equations at each node and every node is treated identically.

This particular derivation of B-splines uses 5th order polynomials and has equal spacings between all of the nodes. The equal node spacing can be a problem in a case like the toroidal shell, where a tendency for discontinuity at certain points requires that a small mesh be used throughout the entire structure. However, the gain in simplicity justifies the extra computation time considering the ease with which problems can be run using up to 1000 elements. The need to use a 5th order formulation stems from the importance of 4th derivatives in the structural equations. When a cubic B-spline representation was tried, poor results were obtained.

The basis function and its derivatives are given by:

$$B_i(x) = \frac{1}{(\Delta x)^5}[(x - x_{i-3})_+^5 - 6(x - x_{i-2})_+^5 + 15(x - x_{i-1})_+^5 - 20(x - x_i)_+^5 + 15(x - x_{i+1})_+^5 - 6(x - x_{i+2})_+^5 + (x - x_{i+3})_+^5] \quad C.2$$

$$B_i'(x) = \frac{1}{(\Delta x)^5}[5(x - x_{i-3})_+^4 - 30(x - x_{i-2})_+^4 + 75(x - x_{i-1})_+^4 - 100(x - x_i)_+^4 + 75(x - x_{i+1})_+^4 - 30(x - x_{i+2})_+^4 + 5(x - x_{i+3})_+^4] \quad C.3$$

$$B_i''(x) = \frac{1}{(\Delta x)^5}[20(x - x_{i-3})_+^3 - 120(x - x_{i-2})_+^3 + 300(x - x_{i-1})_+^3 - 400(x - x_i)_+^3 + 300(x - x_{i+1})_+^3 - 120(x - x_{i+2})_+^3 + 20(x - x_{i+3})_+^3] \quad C.4$$

$$B_i'''(x) = \frac{1}{(\Delta x)^5}[60(x - x_{i-3})_+^2 - 360(x - x_{i-2})_+^2 + 900(x - x_{i-1})_+^2 - 1200(x - x_i)_+^2 + 900(x - x_{i+1})_+^2 - 360(x - x_{i+2})_+^2 + 60(x - x_{i+3})_+^2] \quad C.5$$

where the notation $(f)_+$ is defined by

$$\text{if } (f > 0) \text{ then } (f)_+ = f$$

$$\text{else } (f)_+ = 0 \quad (C.6)$$

Any function u(x) can be defined in terms of the basis functions as

$$u(x) = \sum_i \alpha_i B_i(x) \quad (C.7)$$

Evaluation of the function requires evaluation of the spline function at the point of interest as well as the two nearest neighbors on each side

$$u(x_i) = \alpha_{i-2}B_{i-2}(x_i) + \alpha_{i-1}B_{i-1}(x_i) + \alpha_i B_i(x_i) + \alpha_{i+1}B_{i+1}(x_i) + \alpha_{i+2}B_{i+2}(x_i)$$

$$= \alpha_{i-2} + 26\alpha_{i-1} + 66\alpha_i + 26\alpha_{i+1} + \alpha_{i+2} \quad (C.8)$$

Similarly, the derivatives of u require evaluation of the derivatives of the spline functions at the point and its neighbors

$$u'(x_i) = \alpha_{i-2}B'_{i-2}(x_i) + \alpha_{i-1}B'_{i-1}(x_i) + \alpha_i B'_i(x_i) + \alpha_{i+1}B'_{i+1}(x_i) + \alpha_{i+2}B'_{i+2}(x_i)$$
$$= \frac{1}{\Delta x}(5\alpha_{i+2} + 50\alpha_{i-1} - 50\alpha_{i-1} - 5\alpha_{i+2}) \qquad (C.9)$$

$$u''(x_i) = \alpha_{i-2}B''_{i-2}(x_i) + \alpha_{i-1}B''_{i-1}(x_i) + \alpha_i B''_i(x_i) + \alpha_{i+1}B''_{i+1}(x_i) + \alpha_{i+2}B''_{i+2}(x_i)$$
$$= \frac{1}{(\Delta x)^2}(20\alpha_{i-2} + 40\alpha_{i-1} - 120\alpha_i + 40\alpha_{i+1} + 20\alpha_{i+2}) \qquad (C.10)$$

$$u'''(x_i) = \alpha_{i-2}B'''_{i-2}(x_i) + \alpha_{i-1}B'''_{i-1}(x_i) + \alpha_i B'''_i(x_i) + \alpha_{i+1}B'''_{i+1}(x_i) + \alpha_{i+2}B'''_{i+2}(x_i)$$
$$= \frac{1}{(\Delta x)^3}(60\alpha_{i-2} - 120\alpha_{i-1} + 120\alpha_{i+1} - 60\alpha_{i+2}) \qquad (C.11)$$

APPENDIX D — STRUCTURAL PLOTS FOR DESIGN COMPARISON

D.1 Current Profiles at 20 ms

D.2 Current Profiles at 100 ms

D.3 Inboard Pressure Histories

D.4 Radial Pressure profiles at 20 ms

D.5 Radial Pressure profiles at 100 ms

D.6 Case A Structural Response at 20 ms

D.7 Case B Structural Response at 20 ms

D.8 Case C Structural Response at 20 ms

D.9 Case D Structural Response at 20 ms

D.10 Case A Structural Response at 100 ms

D.11 Case B Structural Response at 100 ms

D.12 Case C Structural Response at 100 ms

D.13 Case D Structural Response at 100 ms

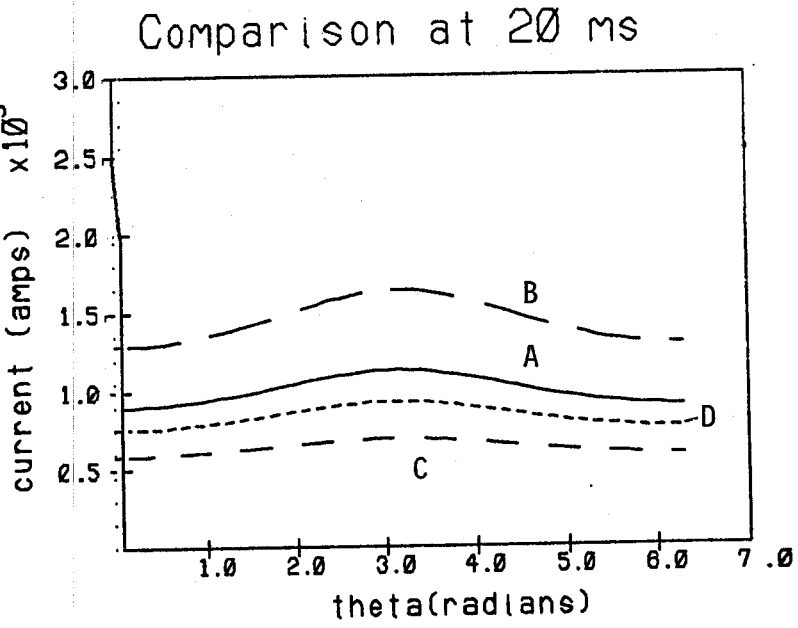

FIGURE D.1

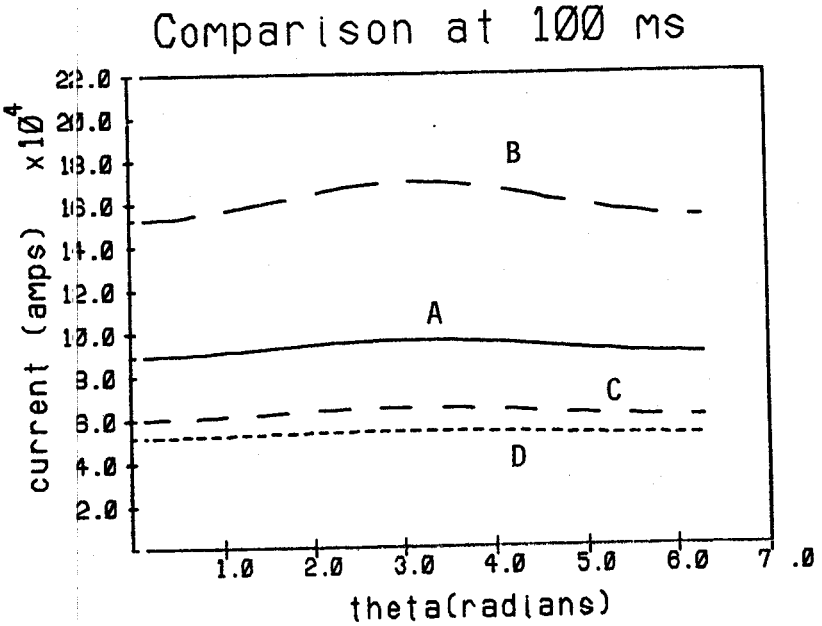

FIGURE D.2

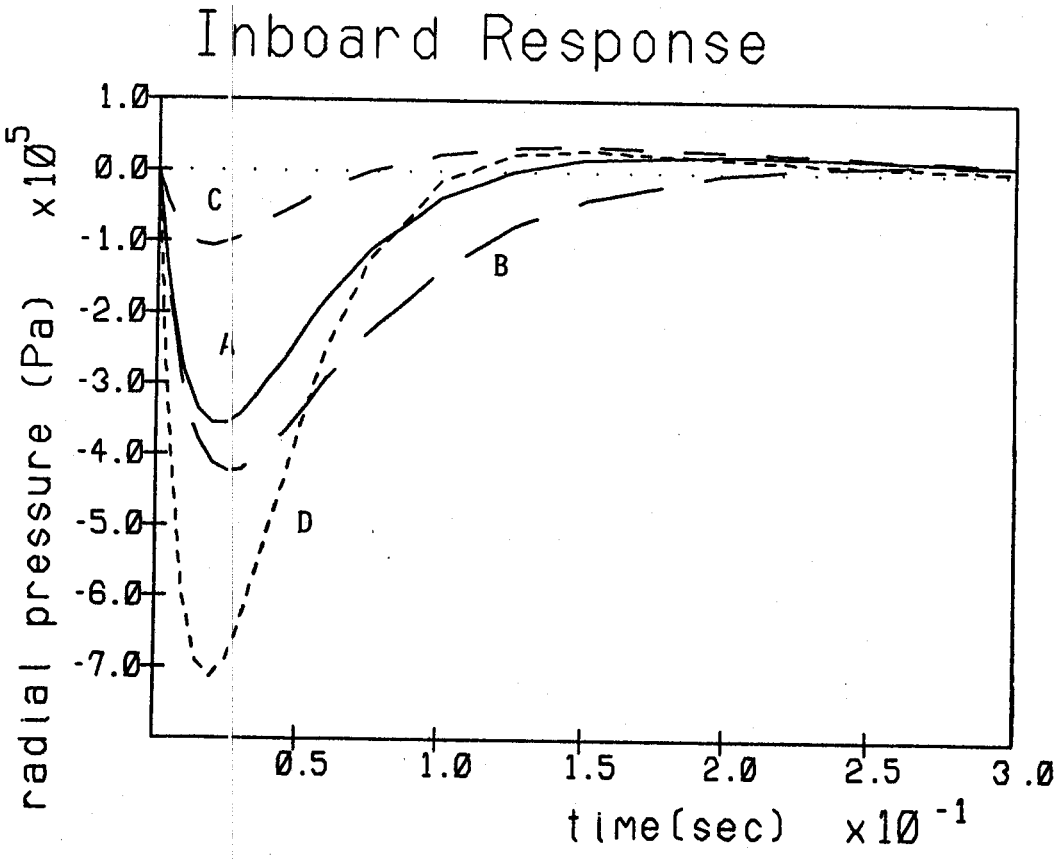
Inboard Response
1.0
0.0
-1.0
-2.0
-3.0
-4.0
-5.0
-6.0
-7.0
radial pressure (Pa) x10^5
C
A
B
D
0.5
1.0
1.5
2.0
2.5
3.0
time(sec) x10^-1

FIGURE D.3

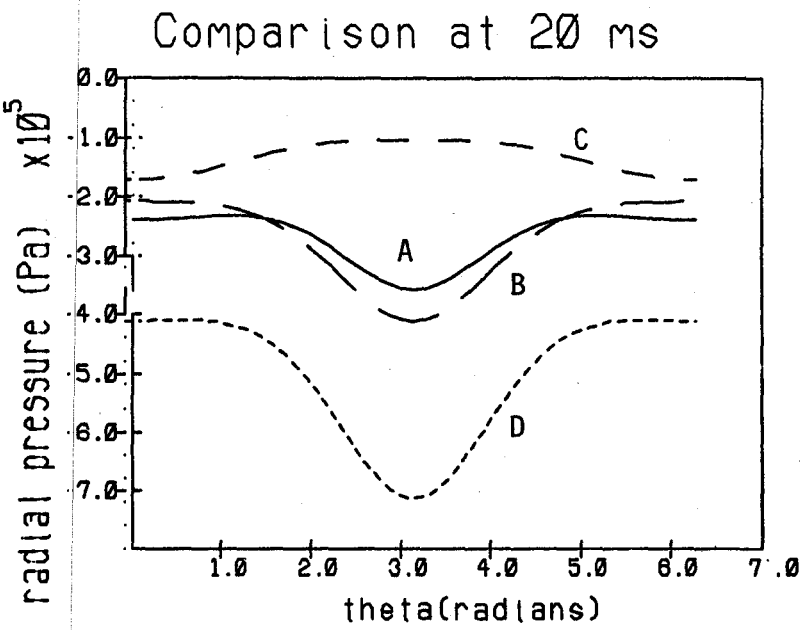

FIGURE D.4

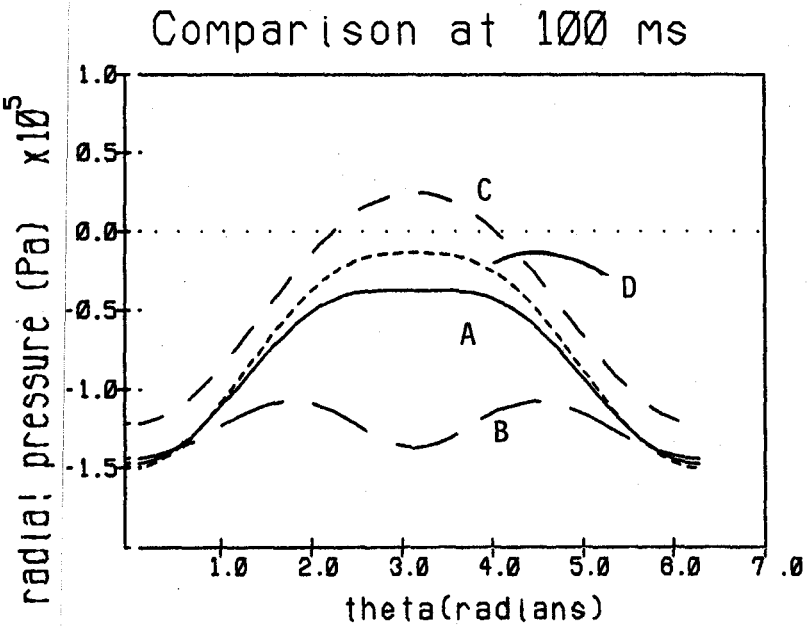

FIGURE D.5

Case A at 20 msec

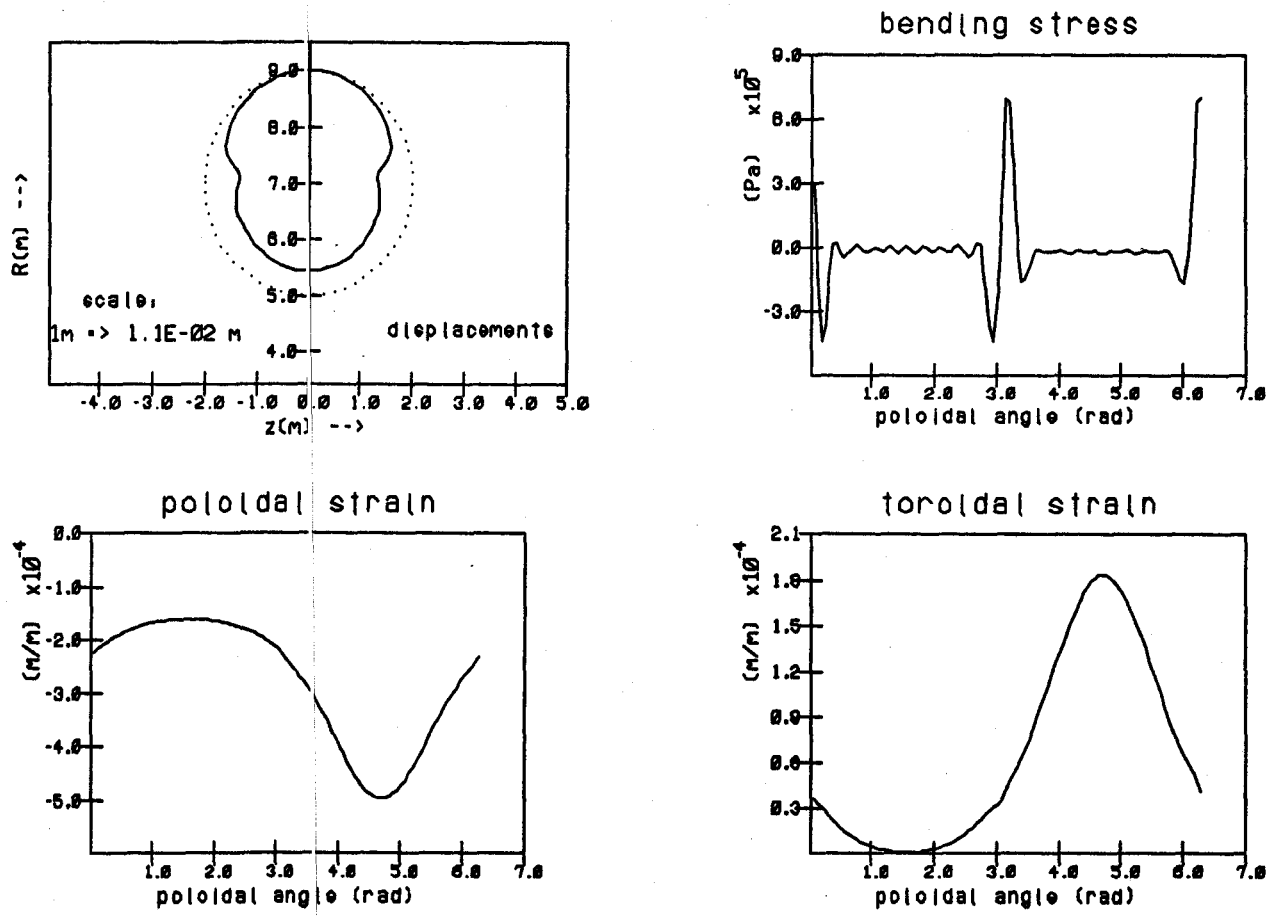

FIGURE D.6

Case B at 20 msec

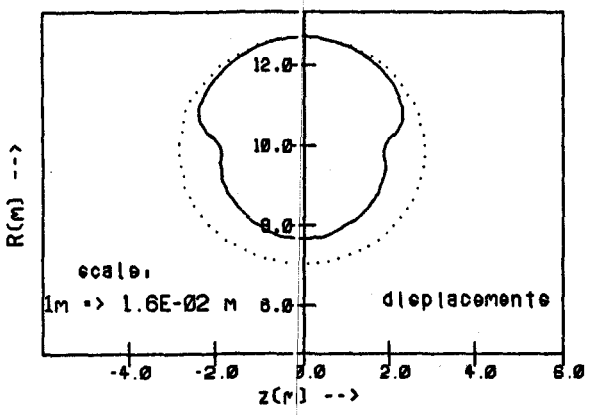

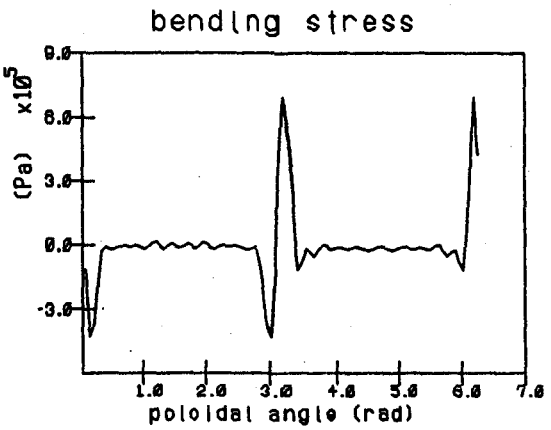

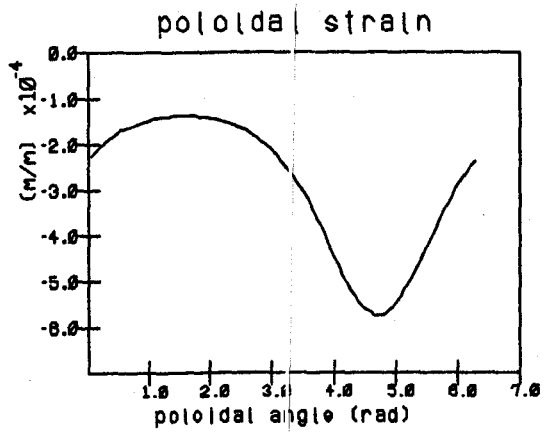

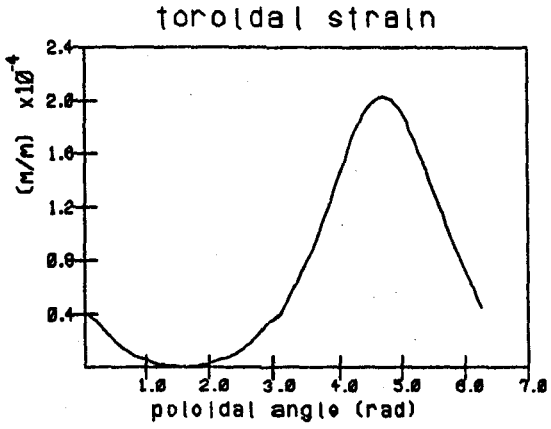

FIGURE D.7

Case C at 20 msec

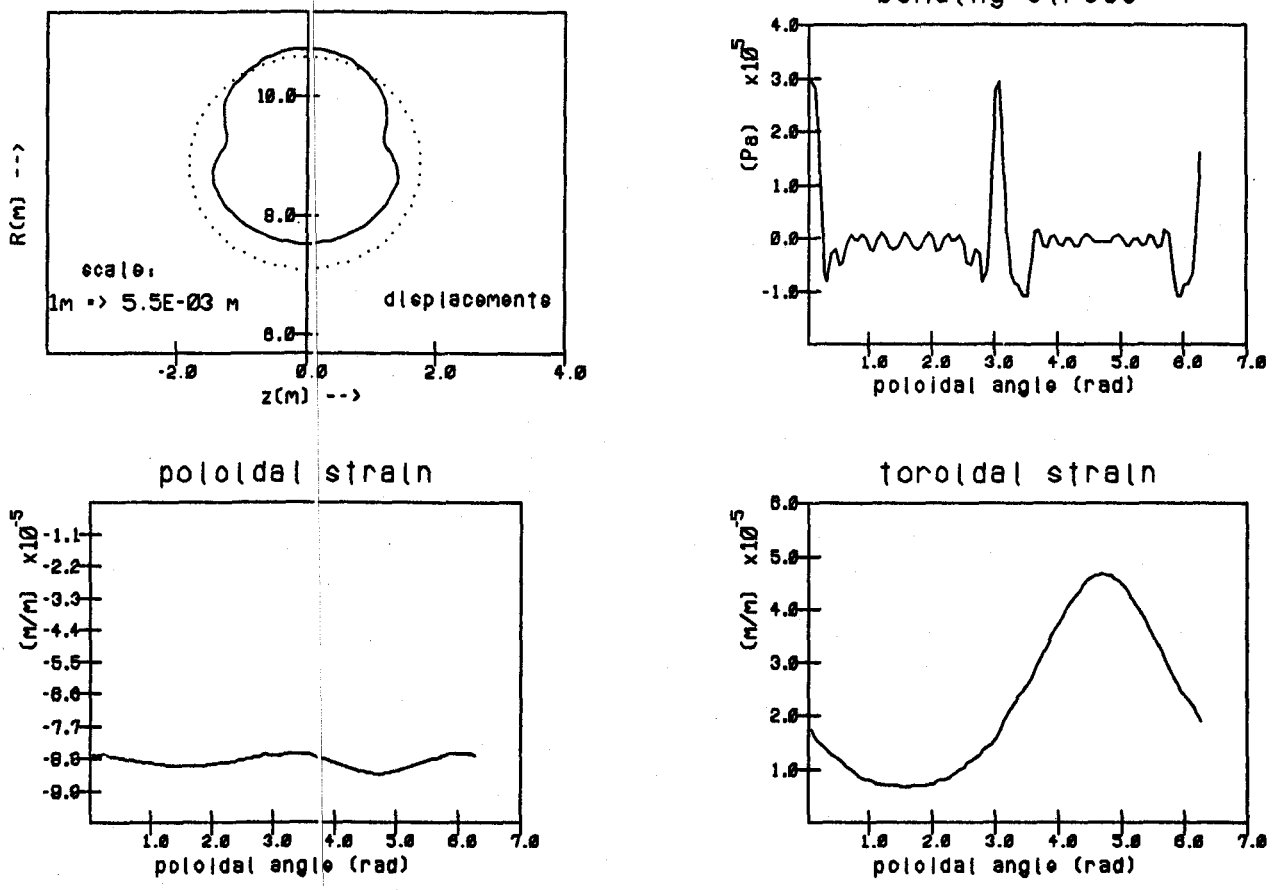

FIGURE D.8

Case D at 20 msec

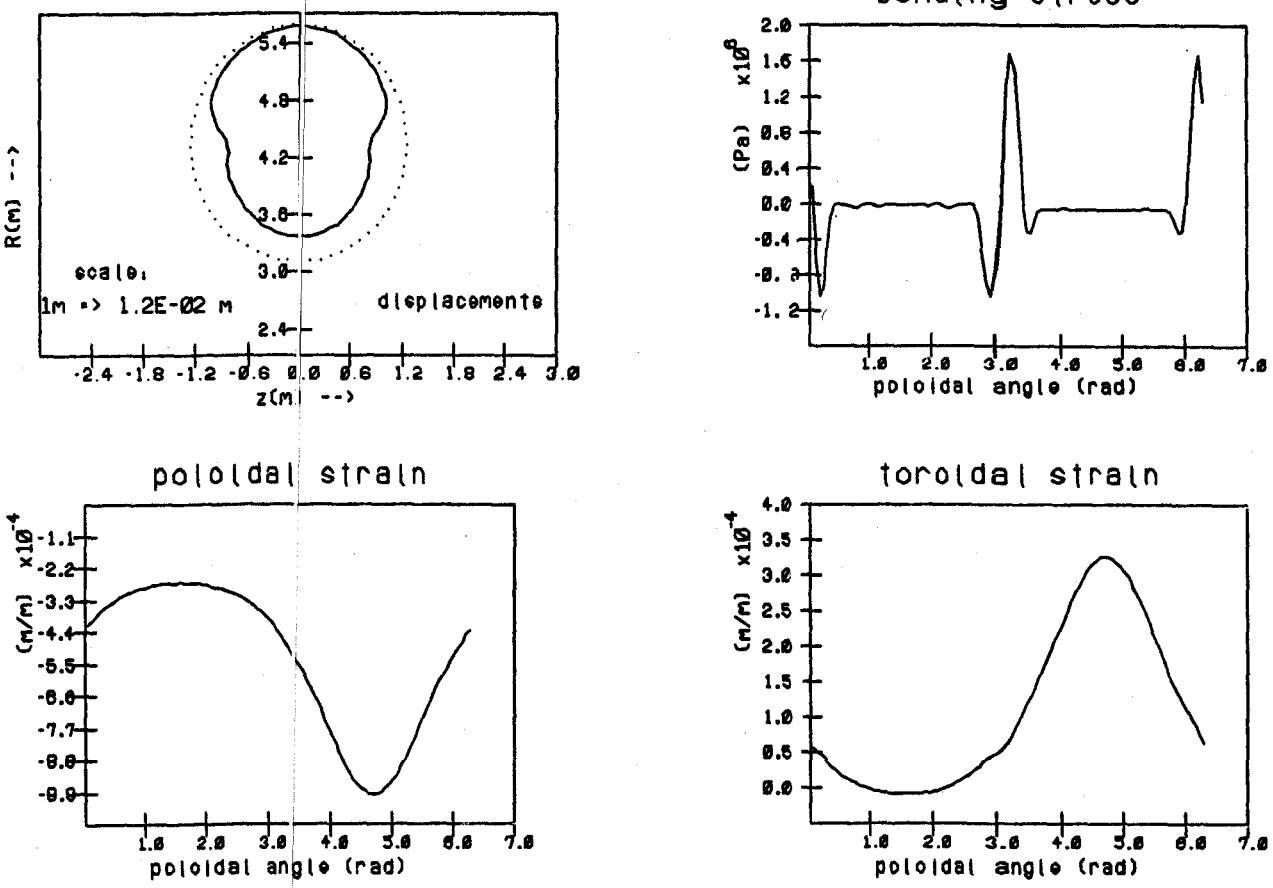

FIGURE D.9

Case A at 100 msec

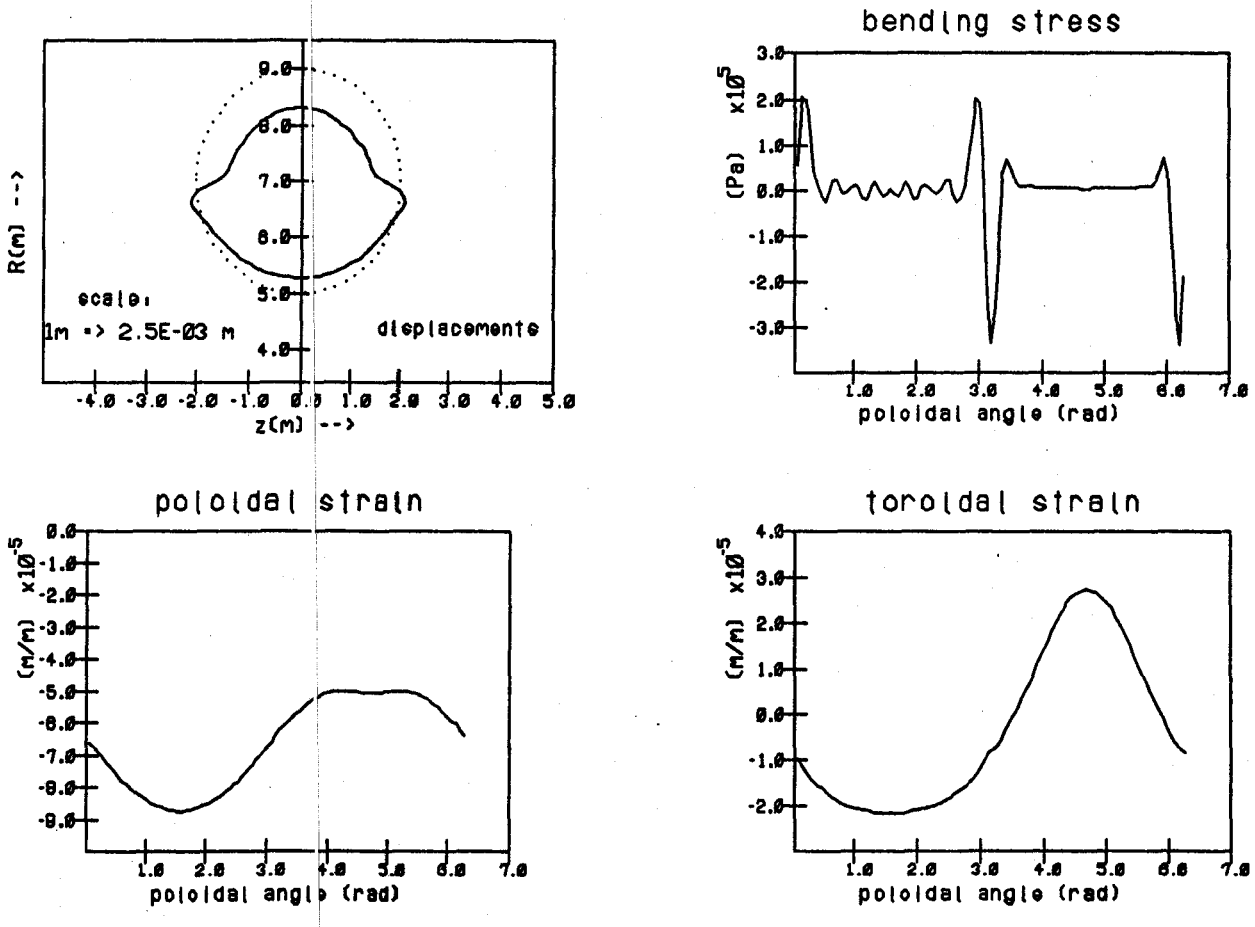

FIGURE D.10

Case B at 100 msec

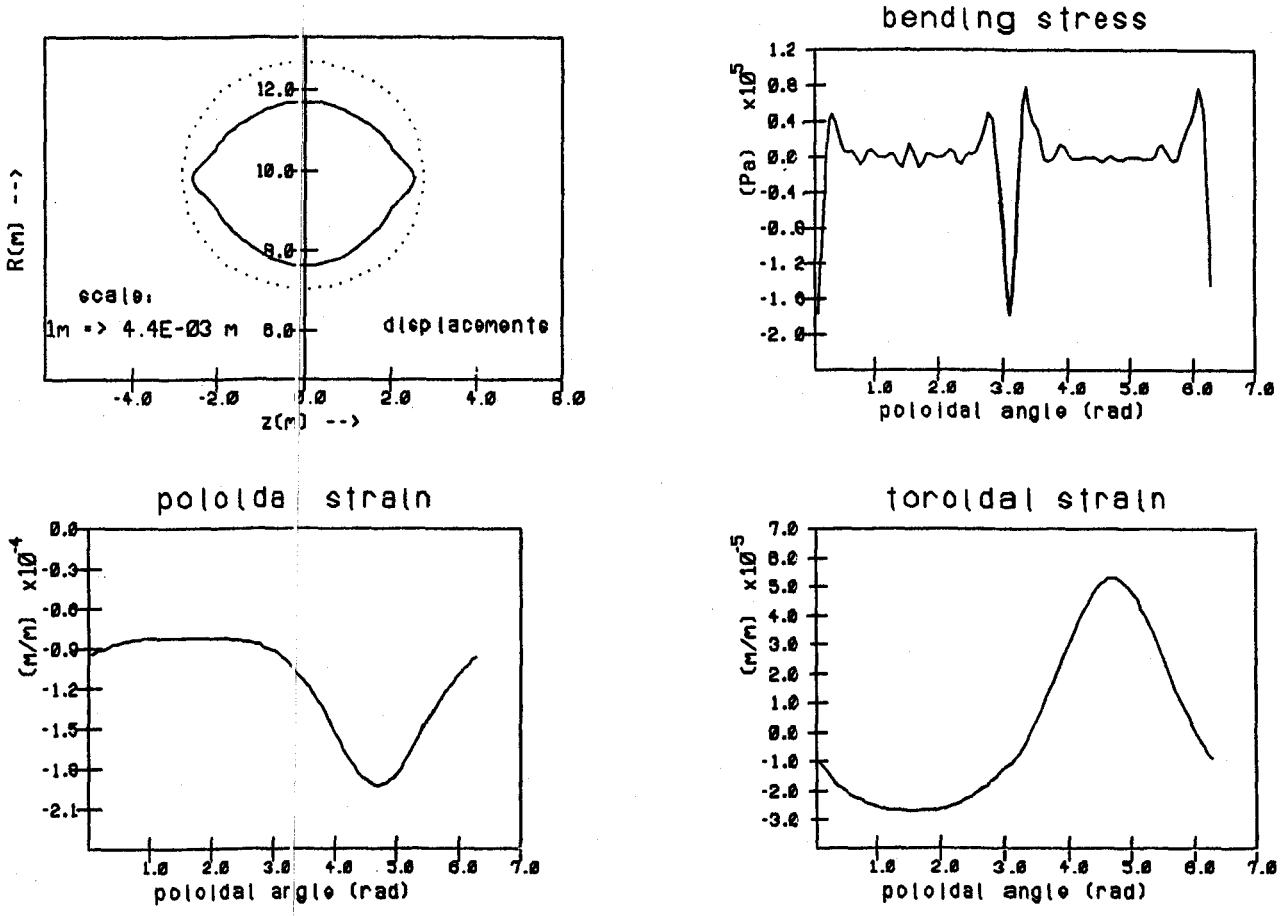

FIGURE D.11

Case C at 100 msec

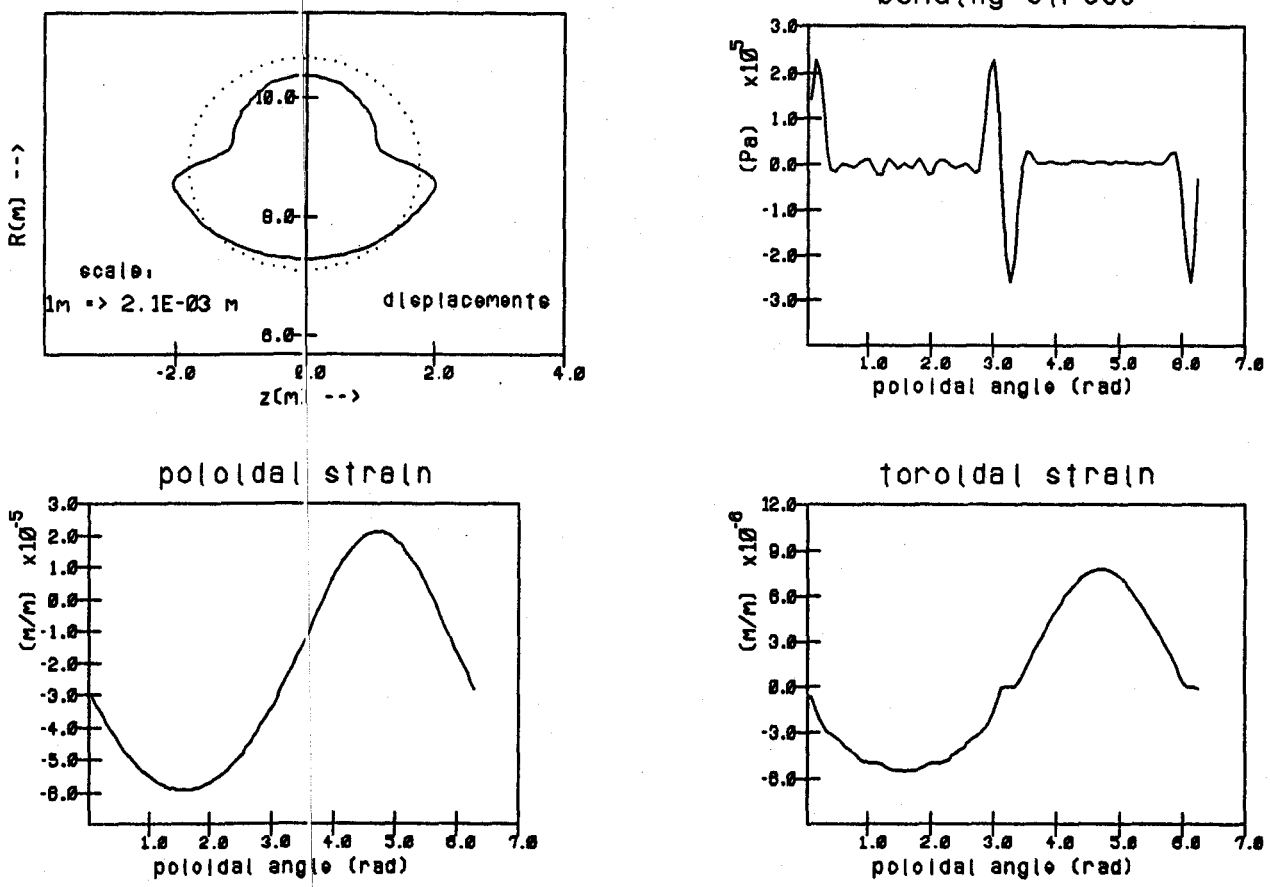

FIGURE D.12

Case D at 100 msec

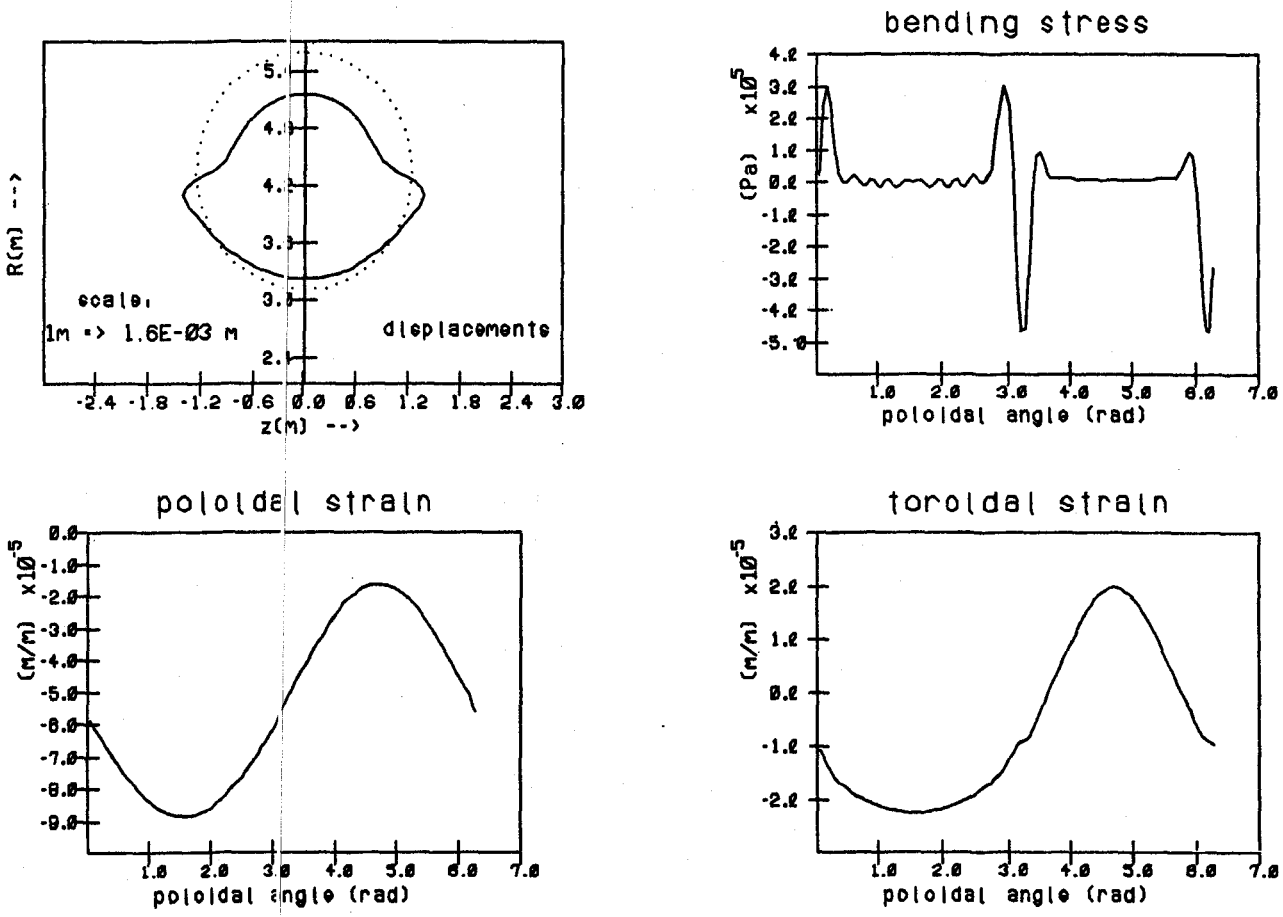

FIGURE D.13